

# Ultrasensitive detection of circulating exosomes with a 3D-nanopatterned microfluidic chip

Peng Zhang<sup>1</sup>, Xin Zhou<sup>1</sup>, Mei He<sup>1,2</sup>, Yuqin Shang<sup>1</sup>, Ashley L. Tetlow<sup>3</sup>, Andrew K. Godwin<sup>3,4</sup> and Yong Zeng<sup>1,4\*</sup>

The performance of current microfluidic methods for exosome detection is constrained by boundary conditions, as well as fundamental limits to microscale mass transfer and interfacial exosome binding. Here, we show that a microfluidic chip designed with self-assembled three-dimensional herringbone nanopatterns can detect low levels of tumour-associated exosomes in plasma (10 exosomes  $\mu\text{l}^{-1}$ , or approximately 200 vesicles per 20  $\mu\text{l}$  of spiked sample) that would otherwise be undetectable by standard microfluidic systems for biosensing. The nanopatterns promote microscale mass transfer, increase surface area and probe density to enhance the efficiency and speed of exosome binding, and permit drainage of the boundary fluid to reduce near-surface hydrodynamic resistance, thus promoting particle-surface interactions for exosome binding. We used the device for the detection—in 2  $\mu\text{l}$  plasma samples from 20 ovarian cancer patients and 10 age-matched controls—of exosomal folate receptor alpha as a potential biomarker for early detection and progression monitoring of ovarian cancer. The nanolithography-free nanopatterned device should facilitate the use of liquid biopsies for cancer diagnosis.

Rapid progress in early-stage diagnostics and precision therapy calls for new tools for the ultrasensitive detection of disease-specific biological particles in bodily fluids, such as circulating tumour cells (CTCs) and extracellular vesicles (EVs)<sup>1–4</sup>. Exosomes—a subtype of EVs secreted by mammalian cells with a typical size range of 30–150 nm—have been implicated in many biological processes, including the immune response, tumorigenesis and metastasis<sup>5,6</sup>. Thus, circulating exosomes are emerging as a new paradigm of ‘liquid biopsy’ for non-invasive cancer diagnosis<sup>4,7</sup>. However, tumour-associated exosomes in biofluids can be very rare during the early stages of disease development. Thus, it is imperative to develop new biosensing capabilities for ultrasensitive and specific analysis of disease-associated exosome subtypes in the background of normal cell-derived vesicles. Current ‘gold standard’ methods for exosome capture and characterization, such as ultracentrifugation and western blot, suffer from poor isolation efficiency, low sensitivity, time-consuming procedures and large sample consumption. Microfluidics has recently been exploited to leverage exosome analysis, but progress in improving sensitivity, speed and multiplicity has been rather limited<sup>3,8</sup>.

Biosensing largely relies on targets interacting with surface-immobilized probes for affinity capture. In such interfacial processes, mass transfer of targets to the surface and the equilibrium and kinetics of binding reactions are the fundamental factors that govern sensing performance<sup>9</sup>. Microfluidics and nanoengineering approaches have been extensively explored to address these limitations. Many micromixing methods, including the herringbone mixer, have been developed to promote microscale mass transfer<sup>10,11</sup>. Two-dimensional (2D) nanoengineering<sup>12</sup> offers an effective means to enhance interfacial binding of biomolecules<sup>13,14</sup>, exosomes<sup>8</sup> and cells<sup>15</sup>. In addition to the limits of mass transfer and binding reaction, it was recently reported that flow stagnation and hydrodynamic resistance due to the non-slip condition at

the liquid–solid interface restrict the convection of slow-diffusing particles to the surface, which significantly reduces binding efficiency<sup>16–18</sup>. To address these boundary effects, a microfluidic chip integrated with three-dimensional (3D) nanoporous microposts was developed by micropatterning carbon-nanotube (CNT) posts inside microchannels. Compared with solid microposts, the nanoporous CNT microposts permit the drainage of liquid through the nanopores, greatly reducing the near-surface flow stagnation and hydrodynamic resistance to enhance surface binding of particles of 40 nm to  $\sim$ 15  $\mu\text{m}$ <sup>16–18</sup>. These studies present a creative strategy for microfluidic integration of 3D nanostructures to overcome the boundary effects; however, the fabrication of 3D CNT patterns is highly sophisticated and time consuming.

As discussed above, previous approaches sought to individually or partially overcome the fundamental limits in mass transfer, surface reaction and boundary effects, which presents a major conceptual constraint in leveraging the biosensing performance. Here, we report an integrated, comprehensive strategy that addresses these three limits simultaneously in one device. Our approach, termed multiscale integration by designed self-assembly (MINDS), exploits microfluidically engineered colloidal self-assembly (CSA)<sup>19</sup> to achieve simple, large-scale integration of 3D nanostructured functional microelements. We used MINDS to combine micropatterning and 3D nanostructuring of a widely used functional microelement herringbone mixer for flow manipulation and molecular recognition. We showed that this 3D nanostructured herringbone (nano-HB) addresses the aforementioned limits in one device (Fig. 1a), as it: (1) effectively promotes microscale mass transfer of bioparticles<sup>20,21</sup>; (2) increases surface area and probe density to enhance binding efficiency and speed; and (3) permits drainage of the boundary layer of fluid through the pores of a nano-HB, which reduces near-surface hydrodynamic resistance<sup>16,17</sup> and enriches particles near the surface to enhance surface binding of particles.

<sup>1</sup>Ralph N Adams Institute for Bioanalytical Chemistry, Department of Chemistry, University of Kansas, Lawrence, KS, USA. <sup>2</sup>Department of Chemical Engineering, University of Kansas, Lawrence, KS, USA. <sup>3</sup>Department of Pathology and Laboratory Medicine, University of Kansas Medical Center, Kansas City, KS, USA. <sup>4</sup>University of Kansas Cancer Center, Kansas City, KS, USA. \*e-mail: [yongz@ku.edu](mailto:yongz@ku.edu)

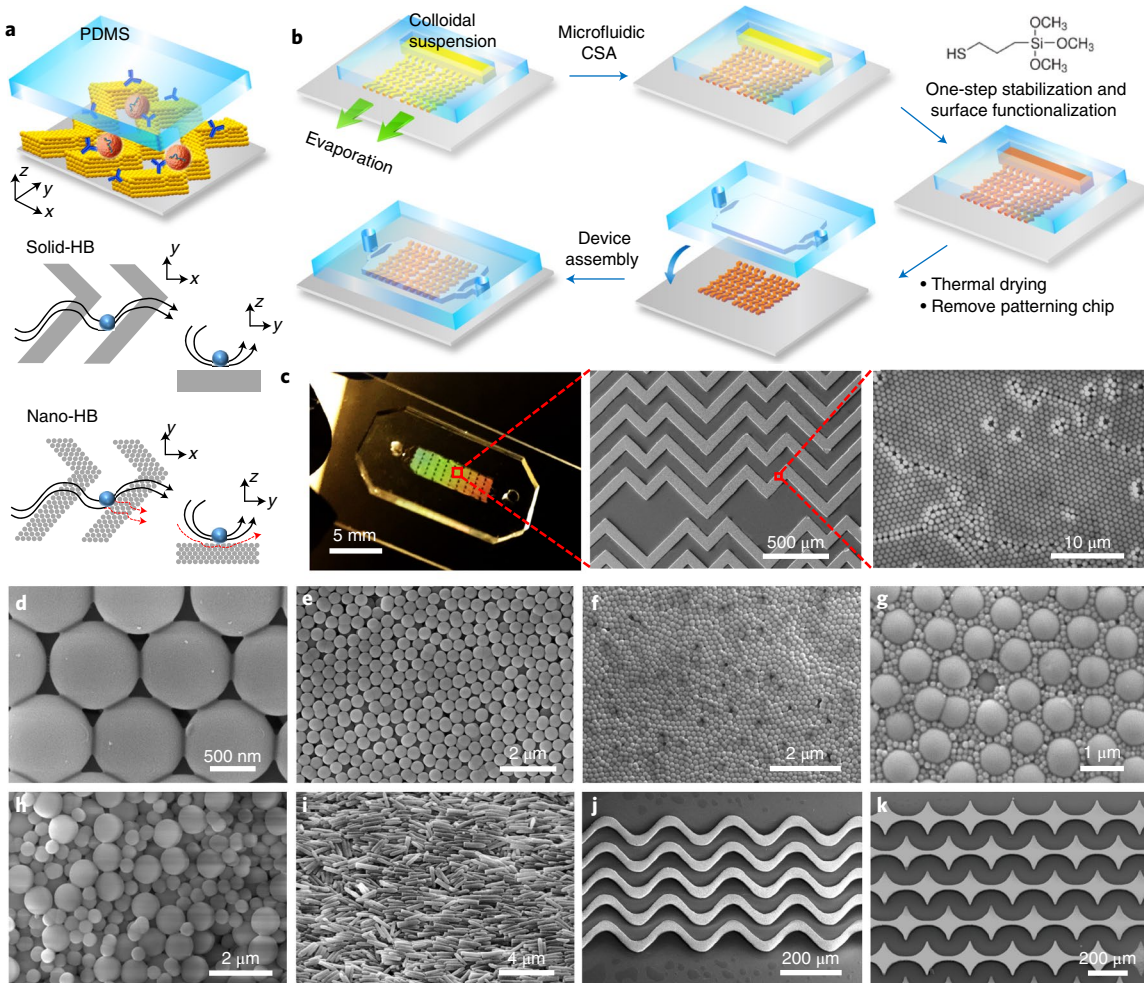


**Fig. 1 | MINDS.** **a**, Schematic of the MINDS strategy that improves biosensing by 3D nanostructuring of microfluidic elements, such as the herringbone mixer. The conventional, solid-HB mixer creates microvortices to promote mass transfer of targets. A particle will experience hydrodynamic resistance near a solid surface that reduces direct surface contact. In a 3D nano-HB chip, fluid near the surface can be drained through the porous structure (red dashed lines) to increase the probability of particle-surface collisions. **b**, Workflow for fabricating a 3D nano-HB chip by MINDS. **c**, A nano-HB chip fabricated with 960 nm silica colloids. Left, digital photo exhibiting Bragg diffraction of light. Middle and right, SEM images at different magnifications showing a high-quality, crack-free herringbone array patterned on a glass substrate with a crystalline nanoporous structure. **d**, Silica necks were formed between the contacting particles by treatment with 5% 3-MPS. **e,f**, SEM images of mono-assembled nano-HBs with silica colloids of 520 (**e**) and 170 nm (**f**). **g**, A well-ordered binary lattice composed of 170 and 960 nm silica colloids at an equal mass ratio. **h**, A randomly organized nano-HB co-assembled with 520 and 960 nm silica colloids at a 1:1 mass ratio. **i**, An anisotropic microstructure assembled from silica nanorods with an average diameter of  $238 \pm 32$  nm and length of  $1.34 \pm 0.26$   $\mu\text{m}$ . **j,k**, Fabrication of crack-free 3D nanostructured sinusoidal ribbon (**j**) and concave diamond arrays (**k**) using designed microfluidic channels to engineer evaporative self-assembly of 960 nm colloids.

As a result, the nano-HB chip afforded an extremely low limit of detection (LOD) of  $10 \text{ exosomes } \mu\text{l}^{-1}$  (200 exosomes per assay) for spiked-in standards, and enabled quantitative detection of low-level exosome subpopulations in blood plasma that are otherwise indiscernible to the conventional flat-channel microfluidic chips. We demonstrated quantitative detection of circulating exosomal CD24, epithelial cell adhesion molecule (EpCAM) and folate receptor alpha (FR $\alpha$ ) markers to detect ovarian cancer using only  $2 \mu\text{l}$  of plasma, indicating the potential applications of our technology to liquid biopsy-based cancer diagnosis.

## Results

**Designable 3D nanostructuring of functional microelements by MINDS.** Fabrication of a MINDS chip is illustrated in Fig. 1b and detailed in the Methods. A nano-HB mixer was constructed using a microchannel network to guide evaporation-driven CSA.

A simple *in situ* treatment with (3-mercaptopropyl) trimethoxysilane (3-MPS) was developed to strengthen the assembled micropatterns and prime the surface for antibody conjugation in one step. After thermal drying and removing the patterning chip, the nano-HB pattern was aligned and sealed with an assay chip with  $\sim 50 \mu\text{m}$  high channels to construct a complete device. Fig. 1c displays a nano-HB chip fabricated by MINDS using 960 nm silica colloids, which exhibited Bragg scattering of light by the embedded colloidal nanostructures. Scanning electron microscopy (SEM) imaging confirmed high-fidelity replication of the channel geometry by the engineered CSA and 3D nanoporous crystalline structures (Fig. 1c). The optimized 3-MPS treatment prevents the formation of cracks during thermal drying and minimizes the mechanical damage caused by removing the patterning chip, while preserving the nanoporosity. This is attributed to the formation of silica necks gluing the contacting nanoparticles by hydrolysis and condensation

reactions of 5% 3-MPS (Fig. 1d). High concentrations of 3-MPS (for example, 10%) can be used to completely fill the pores in nano-HBs (Supplementary Fig. 1), which allows the fabrication of solid herringbone (solid-HB) chips used in the following studies. Meanwhile, 3-MPS functionalizes the surfaces with sulphydryl groups for antibody conjugation via maleimide reaction. Thus, this one-step treatment method greatly simplifies device fabrication.

The MINDS strategy allows us to conveniently engineer the morphology of 3D nano-HBs. We have demonstrated nano-HBs fabricated with a variety of nanomaterials, including mono-assemblies of silica colloids of 960, 520 and 170 nm (Fig. 1d–f), binary nanoparticle combinations (Fig. 1g,h) and silica nanorods (Fig. 1i and Supplementary Fig. 2). Co-assembly of multicomponent mixtures was tuned to create complex morphologies by controlling assembly variables, including the particle size ratio and volume fraction<sup>22,23</sup>. Co-assembly of 170 and 960 nm nanoparticles of an equal volume fraction results in a unique morphology of hexagonally packed large particles surrounded by small particles (Fig. 1g). In contrast, a 960/520 nm nano-HB was found to possess much higher structural disorder and porosity (Fig. 1h). In addition to herringbone patterns, we have demonstrated high-fidelity patterning of complex microelements, such as a sinusoidal channel array previously reported for the immunocapture of CTCs<sup>24</sup> (Fig. 1j) and an array of concave diamonds (Fig. 1k). These results suggest that by utilizing the rich collection of nanomaterials and the flexibility of microfluidic design, the MINDS strategy affords broad applicability for the microscale integration of designable 3D nanostructures to develop new multiscale integrated biosensing systems.

**Fluidic and surface characterization of the nano-HB chip for bioparticle sensing.** We conducted a computational fluid dynamics simulation to study the flow behaviour in the nano-HB chip assembled from 960 nm colloids (see the Supplementary Information for simulation details). The microfluidic herringbone structure has been widely used to promote microscale mass transfer by disrupting the laminar flow in microchannels<sup>10,11</sup>, which is especially important for the efficient capture of cells with low diffusivity<sup>20,21</sup>. We adopted a staggered herringbone geometry of a 225 μm groove pitch and a 125 μm groove width to maximize particle–surface interactions, in accordance with previous studies<sup>25,26</sup>. A mathematical model of the porous domain was defined to resolve the nanoscale structure, while capturing the microscale flow pattern, with reasonable computational effort for this proof-of-concept study. Compared with the flat-channel chip, solid and nano-HB chips enhanced the mixing of two co-flowing aqueous streams with almost the same performance (Fig. 2a). Consistently, close examination of the flow behaviour (Fig. 2b,c) visualized the formation of microvortices by the herringbones, and similar patterns of the transverse and streamwise flows were observed in the two devices. In the nano-HB chip, the pressure-driven fluid can enter the nanoporous domain and exhibits maximum flow rate in the corners and thin surface layer, which was calculated to be less than 0.5% of that of the bulk flow (Fig. 2b,c, insets). This explains that the 3D nanoporous structure does not significantly change the flow mixing behaviour induced by the herringbones (Fig. 2a). It is important to note that such small fluid drainage through the nanoporous domain can disrupt the stagnant boundary layer formed on a solid-HB due to the non-slip condition (Fig. 2b,c, insets, and Supplementary Fig. 3). This effect has been demonstrated to increase particle–surface collisions and thus greatly augment the affinity capture of nano- and microsized particles<sup>17,18</sup>.

The effects of permeability were studied by simulation because this is a critical property of a porous medium that measures the ability to transmit fluids<sup>18,27,28</sup>. With a 100-fold increase in permeability from  $4.7 \times 10^{-15} \text{ m}^{-2}$  to  $4.7 \times 10^{-13} \text{ m}^{-2}$ , no significant change occurs to the bulk flow in a nano-HB channel, while significantly more flow

travels through the nanoporous domains (Supplementary Fig. 4a). Trajectories of 50 nm nanoparticles in the flow were tracked across a unit of 5 herringbone elements. At the low permeability, ~7.6% of the particles can enter the nano-HBs, primarily on the corners; at a 100-fold permeability, this percentage increases to ~16% with more particles travelling through the nanostructures (Supplementary Fig. 4b). This increase in particle–nanostructure interactions again supports the important role of fluid drainage by the nanoporous structure in promoting the boundary mass transport.

We experimentally assessed the enhancement of particle–surface interactions on 3D nano-HBs. The chips used here contain 25-μm-tall nano-HBs assembled from 960 nm particles, which possess pore sizes of >144 nm (15% of the particle size), as estimated from the perfect face-cubic centred structure. Figure 2d shows that the solid- and nano-HB chips exhibited similar performance with regard to creating transverse flow across the channels to mix 2 streams of 46 nm fluorescent nanoparticles and phosphate-buffered saline (PBS). This observation agrees well with the simulation result that the porous structure does not significantly affect the ability of 960 nm herringbones to create microvortex mixing (Fig. 2a). It is noted that the numerical simulation underestimates the flow penetration into the nano-HBs because the actual self-assembled colloidal crystals are more porous than the perfect face-cubic centred structure (Fig. 1c–f). To assess the flow penetration in the nano-HB, we injected the fluorescent nanoparticles through a chip at a constant flow rate of  $0.5 \mu\text{l min}^{-1}$  and monitored the fluorescence intensity inside the nanostructure and the open groove regions near the centre of the microchannel. As shown in Fig. 2e and Supplementary Fig. 5a, the signals in the grooves and nanostructures increased gradually and approached steady levels within ~60 and ~90 s, respectively. In contrast, only a slight increase in fluorescence intensity was observed in the solid-HBs, which was attributed to the solution flowing above the microstructures (Fig. 2f and Supplementary Fig. 5b). We also used confocal fluorescence microscopy to verify the flow penetration. Representative 3D images constructed from scanning the herringbone patterns (25 μm tall) for a depth of 20 μm from the substrate (Fig. 2e,f) confirm the penetration of nanoparticles into the surface layers of nano-HBs. For comparison, we carried out a diffusion experiment on the nano-HB chip in which the fluorescent nanoparticle solution was stopped once it entered the observation window, and the diffusion of nanoparticles from the groove into the nanostructures was monitored for 60 min (Fig. 2g). The fluorescence signal in the grooves decreased slowly, indicating that the nanoparticles were diffusing downstream. The fluorescence level in the adjacent nanostructure increased at a rate much slower than that driven by the constant flow (Fig. 2e). These findings verify hydrodynamic flow as the primary mechanism driving the transport of nanoparticles into nano-HBs.

Moreover, it was seen that, in contrast with solid-HBs, nano-HBs concentrate nanoparticles in the stream on their surface and the region beneath (Fig. 2h and Supplementary Fig. 5), in line with the simulated flow pattern in nano-HBs (Fig. 2b,c). This is attributed to the penetrating flow increasing the flux of particles into the nano-HBs, which retain nanoparticles like a sieve. Particle enrichment at the binding interface will improve capture efficiency as it enhances surface interactions and favourably shifts the reaction equilibrium. We also verified that analyte particles and particulate objects in human plasma will not be permanently trapped inside nano-HBs to block the flow penetration and cause non-specific signals (Supplementary Fig. 6). This could be attributed to the unique porous structure of nano-HB in which the ‘through pores’ defined by the packed colloids are all interconnected to form a 3D ‘nanochannel’ network without dead ends. Overall, our results reflect the advantages of our 3D nanoengineering approach; not only does it increase the binding surface area, but it also overcomes the boundary effects for bioparticle sensing. Slight flow penetration was also

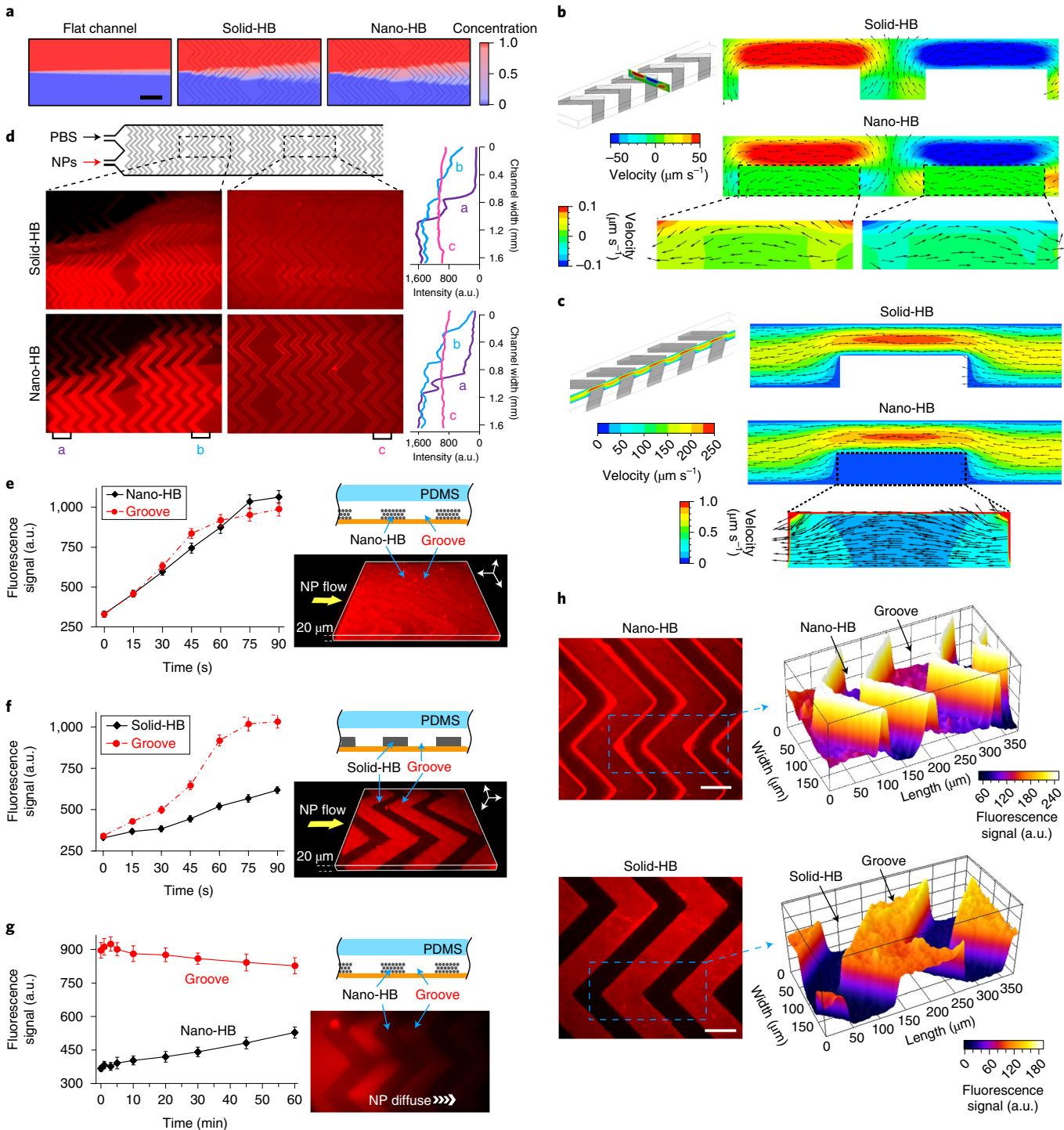


**Fig. 2 | Fluidic characterization of nano-HB chips.** **a**, Simulation of mixing 2 streams of 50 nm nanoparticles (NPs) and water co-flowing at  $1\text{ }\mu\text{l min}^{-1}$  in a flat-channel, solid-HB or nano-HB device. A magnified view over the first two herringbone units is shown. Scale bar, 400  $\mu\text{m}$ . **b,c**, Simulation results showing the transverse flow profiles across the channel width (**b**) and the streamwise flow profiles along the channel length (**c**). Insets, flow patterns inside the nanoporous domains. Colour contours indicate the velocity magnitude, while vectors represent the flow direction. The flow rate was  $0.5\text{ }\mu\text{l min}^{-1}$ . **d**, Fluorescence images (left) and transverse intensity plots (right) of mixing 2 flows of 46 nm fluorescent NPs and PBS injected at  $0.25\text{ }\mu\text{l min}^{-1}$  in parallel. The intensity plots were measured along the channel width at three positions, as indicated in the images. **e,f**, Left, time-lapse plots of fluorescence intensity measured in the herringbone structures and open grooves when a solution of 46 nm fluorescent NPs was pumped through a nano-HB (**e**) or solid-HB chip (**f**) at  $0.5\text{ }\mu\text{l min}^{-1}$ . Right, 3D confocal fluorescence microscopy images were acquired when the channels were filled with the NP solution. **g**, Left, time-lapse monitoring of the diffusion of 46 nm NPs from the grooves into nano-HB structures. Flow pumping was stopped when the NP solution entered the observation region. Right, a fluorescence image was acquired at  $t=60\text{ min}$ . **h**, Left, representative 2D confocal microscopic images of the nano-HB (top) and solid-HB structures (bottom), with the NP solution flowing through the channels. These images were acquired at approximately  $15\text{ }\mu\text{m}$  below the herringbone surface. Right, partial surface plots of the images are displayed for the areas indicated by the dashed rectangles. Scale bars,  $100\text{ }\mu\text{m}$ . In **e–h**, nano-HB chips were assembled with 960 nm silica colloids. Error bars represent 1 s.d. ( $n=3$ ).

observed in the CNT microposts with ~80 nm pores, which greatly enhances the capture of virus-sized particles, bacteria and cells<sup>16,17</sup>.

In addition to mass transfer and boundary effects, surface properties such as surface probe density are important variables that govern the performance of biosensing<sup>9,12</sup>. To this end, we assessed the functionalization of nano-HBs made of 960 nm silica colloids with anti-CD81 monoclonal antibody. Using 3D confocal fluorescence microscopy, we verified that the internal surface of 3D nano-HBs was conjugated with CD81 monoclonal antibody (Supplementary Fig. 7a–c). Compared with a flat glass substrate, the nano-HB chip was found to increase the number of immobilized antibodies 3.25-fold (Supplementary Fig. 7d,e). Such enhancement in the probe density and accessible surface areas will promote the thermodynamics and kinetics of surface binding, and thus improve the sensitivity and speed of target capture and detection. Collectively, our fluidic and surface characterization studies suggest that the nano-HB chip enabled by the MINDS strategy provides a designable multiscale engineered system to improve biosensing by overcoming the fundamental limits in mass transfer, surface reaction and boundary effects in one device. As a proof of concept, we evaluated the device as a diagnostic exosome analysis system for the liquid biopsy-based detection of cancer.

**Evaluation of exosome immunocapture on a nano-HB chip.** First, we assessed the nano-HB chip for exosome immunocapture using the well-characterized EV standards isolated from a colon cancer COLO-1 cell line<sup>8</sup>. Compared with a bovine serum albumin (BSA)-coated chip, an anti-CD81 monoclonal antibody modified chip was shown to capture far more exosomes (Fig. 3a) from a 20 µl spiked-in sample ( $10^5 \mu\text{l}^{-1}$  in PBS), indicating good immunocapture specificity. The captured exosomes displayed typical spherical or cup shapes and formed clusters (Fig. 3b), consistent with previous findings<sup>29,30</sup>. We estimated the sizes of vesicles captured on nano-HB chips ( $n > 300$ ) from 10 SEM images, which displayed a notably smaller size distribution (40–160 nm) than that of ultracentrifugation-isolated EVs, as measured by nanoparticle tracking analysis (NTA) (Fig. 3c). The size range of EVs observed with the nano-HB immunocapture agrees with that of the standard magnetic bead immunocapture<sup>31</sup>. To investigate exosome capture in a complex matrix, we performed nano-HB capture of 3,3'-dioctadecyloxacarbocyanine perchlorate (DiO) dye-stained COLO-1 EVs spiked in tenfold-diluted healthy human plasma. With confocal fluorescence microscopy, COLO-1 exosomes were seen to be captured mostly within the top layers of several micrometres deep, with a decreasing density gradient inwards (Fig. 3d and Supplementary Fig. 8). Such spatial distribution of captured exosomes is in line with the simulated flow patterns in nano-HBs (Fig. 2b,c), confirming flow penetration into the 3D nanopore structures. Given that unlabelled plasma exosomes were also captured, our observation indicates that the binding events on the walls do not block the nano-HBs, presumably due to their large number of pores and the enhanced transport of nanovesicles driven by the penetrating flow.

We evaluated the capture capacity and efficiency of nano-HB chips by monitoring the volume of exosomes depleted from the sample solution flowing through the nano-HB chip<sup>32</sup>. To this end, DiO dye-stained COLO-1 EVs were spiked in either PBS or tenfold-diluted patient plasma at  $10^6 \mu\text{l}^{-1}$  and injected continuously into the BSA- or CD81 monoclonal antibody-coated chips at  $0.5 \mu\text{l min}^{-1}$ . Then, 2 µl of eluent was sampled at the outlet every 15 min and measured with a microvolume plate reader to determine the decrease in fluorescence intensity ( $\Delta\text{FL}$ ) caused by exosome depletion relative to the signal level of the sample before capture (Fig. 3e). A very small  $\Delta\text{FL}$  was observed on the BSA-coated chips ( $5.5 \pm 0.98\%$  of the original sample for PBS and  $5.3 \pm 1.1\%$  for plasma media), indicating minimal matrix effects on the nano-HB chip. Exosome capture on the antibody-modified chips constantly resulted in a high

$\Delta\text{FL}$  ( $95 \pm 2\%$ ) for spiked PBS over 250 min injection (that is, an accumulated sample volume of 125 µl). The plasma was estimated to contain  $>10^{10} \text{ EVs ml}^{-1}$  by ultracentrifugation and NTA. These unlabelled vesicles and other particulate species in plasma compete for flow access into nano-HBs and/or surface binding sites. Despite the vast background, a consistent  $\Delta\text{FL}$  of 86–92% was observed for capturing exosomes spiked in diluted plasma over a loaded volume of up to 82 µl, while  $\Delta\text{FL}$  remained at 75% at 100 µl. Thus, the current nano-HB chip affords sufficient capacity for sensitive and quantitative analysis of up to 10 µl undiluted plasma. If needed, the capture capacity can be readily expanded by scaling up the chip size or the number of channels.

Based in the measurements in Fig. 3e, the specific capture efficiency of our nano-HB chip can be estimated by subtracting the non-specific  $\Delta\text{FL}$  measured by the BSA-coated chip from that obtained for exosome immunocapture to calculate the percentage of the corrected  $\Delta\text{FL}$ . Using this approach, we determined the specific capture efficiency of the nano-HB chip for fluorescently stained EVs of various cancer cell lines spiked in healthy plasma: COLO-1 ( $85.0 \pm 3.2\%$ ); MCF-7 ( $81.3 \pm 4.1\%$ ); and SKOV3 ( $84.1 \pm 3.5\%$ ) (Fig. 3f). For comparison, standard ultracentrifugation isolation only recovered  $15.5 \pm 1.7\%$  of fluorescent COLO-1 EVs spiked in healthy plasma, in line with previously reported values<sup>33,34</sup>.

The capture performance of the nano-HB chip was further evaluated for downstream analysis of the messenger RNA (mRNA) content of exosomes using the commercial droplet digital PCR (ddPCR) technique. Here, we focused on two ovarian cancer cell lines, SKOV3 and OVCAR3, which are commonly used in vitro cell culture models representative of high-grade serous ovarian cancer—the most aggressive subtype that accounts for nearly two-thirds of all ovarian cancer-related deaths<sup>35</sup>. Designed for non-invasive cancer diagnosis using small sample volumes (<100 µl; Fig. 3e), our microfluidic device has limited preparative sample processing capacity for bulk mRNA analysis; thus, we used EVs isolated and concentrated by ultracentrifugation for on-chip immunocapture to yield sufficient exosomes for off-chip RNA extraction, complementary DNA (cDNA) synthesis and ddPCR, following the established protocols<sup>4,36</sup> (see Methods for more information). To assess the capture efficiency,  $100 \mu\text{l}$  ultracentrifugation-concentrated SKOV3 and OVCAR3 EVs ( $10^6 \mu\text{l}^{-1}$ ) were run on the chips and the captured exosomes were eluted out for ddPCR quantification of GAPDH mRNA (Fig. 3g). The GAPDH mRNA levels in chip-captured exosomes were measured to be  $76.5 \pm 2.6\%$  for SKOV3 and  $80.1 \pm 5.0\%$  for OVCAR3, relative to the initial samples. The capture efficiency for SKOV3 exosomes is slightly lower than that measured by the fluorescence detection method in Fig. 3f, which may be attributed to the RNA loss and degradation during multistep exosome elution and RNA extraction. To assess the nano-HB chip for exosomal mRNA profiling compared with ultracentrifugation isolation, we detected six tumour-associated markers that have been identified in ovarian cancer-derived exosomes<sup>4</sup>: human epidermal growth factor receptor 2, epidermal growth factor receptor, FRA, CA125, EpCAM and CD24. The combined assay of on-chip purification and ddPCR analysis reported mRNA patterns consistent with that of the ultracentrifugation-purified SKOV3 and OVCAR3 EVs, respectively (Fig. 3h and Supplementary Fig. 9). These results further demonstrate the validity of the nano-HB chip for exosome immunocapture. The high capture efficiency of the nano-HB chip compares favourably with recently reported methods<sup>32,33,37</sup>, permitting sensitive exosome detection.

**Ultrasensitive detection and quantitative protein profiling of exosomes.** The nano-HB chip combined with a sandwich exosome enzyme-linked immunosorbent assay (ELISA) method<sup>8</sup> was implemented and optimized for the sensitive and specific detection of tumour-derived exosomes. CD81 provided high capture efficiency

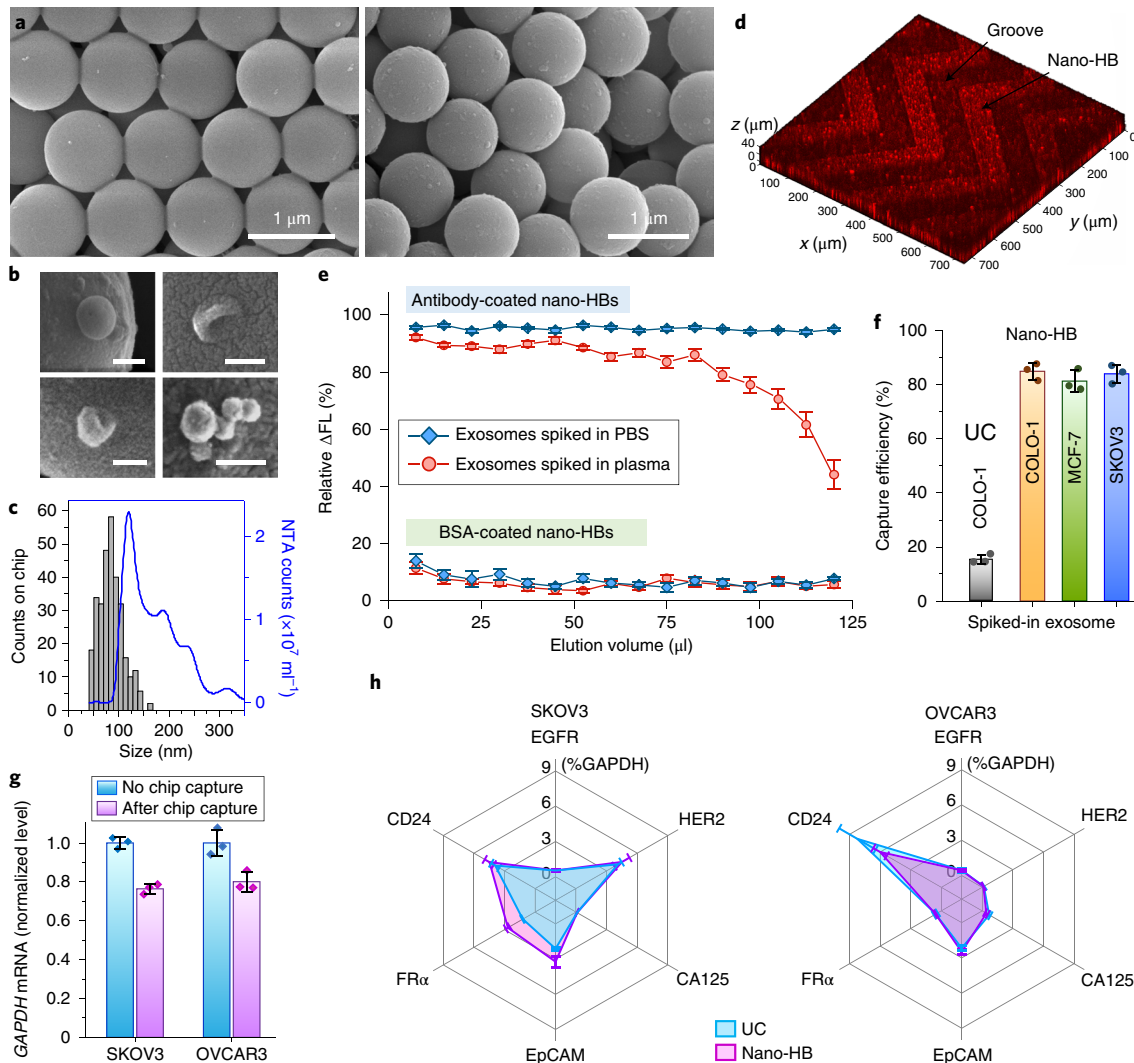


**Fig. 3 | 3D-engineered nano-HB chip affords efficient immunocapture of exosomes.** **a**, SEM images showing minimal non-specific absorption and immunocapture of COLO-1 exosomes ( $10^5 \mu\text{l}^{-1}$ ) on a non-modified (left) and monoclonal antibody-coated device (right). **b**, Typical sphere- and cup-shaped morphologies, and clusters of COLO-1 exosomes captured on nano-HBs. Scale bars: 100 nm. **c**, Representative size distribution of nano-HB-captured COLO-1 exosomes ( $n > 300$ ) measured by SEM, compared with NTA analysis of ultracentrifugation (UC)-isolated vesicles. **d**, 3D confocal fluorescence microscopy showing exosomes captured inside nano-HBs. DiO-stained COLO-1 cell-derived exosomes were spiked in human plasma ( $10^5 \mu\text{l}^{-1}$ ). **e**, Immunological and non-specific capture of COLO-1 exosomes as a function of the injected sample volume, assessed using a monoclonal antibody or BSA-coated nano-HB chip, respectively. DiO dye-stained exosomes were spiked in PBS or tenfold-diluted human plasma ( $10^6 \mu\text{l}^{-1}$ ) and injected continuously through the chips at  $0.5 \mu\text{l min}^{-1}$ , and  $2 \mu\text{l}$  eluent was collected at the outlet every 15 min and measured by a microvolume plate reader to determine the reduction in the fluorescence signal with respect to that of the original sample. **f**, Comparison of standard UC isolation and nano-HB capture of fluorescently stained exosomes of various cancer cell lines spiked in healthy plasma ( $10^6 \mu\text{l}^{-1}$ ). The signal decrease caused by exosome immunocapture was measured as in **e**, and that of non-specific adsorption was subtracted, to calculate the percentage of corrected signal reduction (that is, the specific capture efficiency). **g**, Capture efficiency of nano-HB chips as measured by GAPDH mRNA levels. EVs isolated and concentrated from SKOV3 and OVCAR3 cell culture media by UC were spiked in PBS ( $10^6 \mu\text{l}^{-1}$ ), and  $100 \mu\text{l}$  of the solution was run on the chip. Captured exosomes were eluted out for ddPCR quantification. The GAPDH mRNA levels in chip-captured exosomes were normalized by the level in the same amount of EVs measured without chip capture. **h**, Profiles of six mRNA markers measured in the chip-captured SKOV3 and OVCAR3 exosomes compared with the vesicles isolated and concentrated by UC. Exosome capture and elution on the nano-HB chip was performed as in **g**, and the levels of individual mRNAs measured by ddPCR were normalized against GAPDH. Anti-CD81 monoclonal antibody was used for exosome capture in all cases. EGFR, epidermal growth factor receptor; HER2, human epidermal growth factor receptor 2. Error bars represent 1 s.d. ( $n=3$ ).

for exosomes derived from various cancer cell lines (Fig. 3e–g). Thus, our assay was designed to capture overall exosomes by anti-CD81 monoclonal antibody and to detect surface protein markers with specific monoclonal antibodies, assisted by fluorogenic signal amplification to further enhance the sensitivity. With the COLO-1 exosome standards, we have systematically examined the critical conditions for the immunoassay and enzymatic signal amplification,

including the washing buffer, concentration of reporter enzyme and reaction time, to afford the maximum signal-to-noise ratio (Supplementary Fig. 10a–c). We also verified that there is no endogenous  $\beta$ -galactosidase activity from exosomes that would interfere with the enzymatic fluorogenic detection (Supplementary Fig. 10d), which could be due to  $\beta$ -galactosidase not being present on the exosome membrane. The established protocol affords specific exosome

detection on the antibody-modified chip, as verified by the low non-specific background obtained using the PBS blank as the control sample and a control chip coated with BSA or normal human immunoglobulin G (IgG) (Supplementary Figs. 10e,f and 11a).

As the porous structure has significant effects on interfacial sensing, we evaluated the nano-HBs engineered with distinct morphologies, as shown in Fig. 1d–i, for exosome detection (Fig. 4a). Substantial signal enhancement was observed when shifting from the 170 nm herringbone with ~26 nm pores to the 960 nm herringbone with ~144 nm pores, owing to the enhanced flow penetration that augments exosome–surface interactions and the accessibility to the internal binding surface. The nanorod-HBs yielded a lower signal than 520 nm particles, which can be attributed to the lower porosity of well-aligned, tightly packed rods (Fig. 1i) compared with close-packed monodisperse spheres<sup>38</sup>. Random packing of 520 and 960 nm particles led to larger pores than the ordered mono-assemblies (Fig. 1h), and therefore a better detection sensitivity. Decreasing signal levels were obtained for the 520/170 nm and 960/170 nm structures, in agreement with the finding that increasing the particle size ratio improves the order of packing, but reduces the porosity and pore sizes<sup>22,23</sup>. Compared with the close-packed array of monodispersed nanoparticles, precise control of multi-component CSA is more difficult<sup>22</sup>, and highly porous, randomly packed structures result in reduced mechanical strength. Thus, we selected the 960 nm herringbone for subsequent studies as it offers a combination of high sensitivity and ease of fabrication. In addition to the morphology, we also optimized the geometry of nano-HBs. Using the MINDS strategy, the microscale geometry of nano-elements can be directly manipulated by designing the moulding channels (Fig. 1j,k). Here, we adopted a well-established herringbone design of 100 μm width and 225 μm pitch from previous studies<sup>25,26</sup>, and investigated nano-HBs of 15–35 μm height embedded in a 50-μm-tall channel. The 25 μm height was found to provide the best flow mixing efficiency and the highest signal-to-noise ratio for exosome detection (Supplementary Fig. 12).

With the optimized chip design and assay conditions, we calibrated and compared the nano-HB chips with the flat-channel and solid-HB devices for quantitative exosome detection (Fig. 4b and Supplementary Fig. 13). A mixture of anti-CD9, CD63 and EpCAM monoclonal antibodies was used to quantify the overall exosomes captured on the chip (Supplementary Table 1). The flat-channel chip yielded a theoretical LOD of  $5.0 \times 10^4$  EVs  $\mu\text{l}^{-1}$ , as calculated from the mean blank signal plus three standard deviations ( $n=3$ ). The solid-HB chip afforded a much lower LOD of  $3.2 \times 10^2$   $\mu\text{l}^{-1}$ , as a result of its substantially better mixing efficiency and larger surface area. 3D nano-HB chips further reduced the LOD to  $10 \mu\text{l}^{-1}$  (that is, 200 vesicles in a 20  $\mu\text{l}$  sample; Fig. 4b, inset), and expanded the dynamic range over 4 orders of magnitude. Considering that the solid-HB also has a nanostructured exterior surface (Supplementary Fig. 1), this direct comparison with the solid-HB assay provides evidence that the enhancement in sensitivity arises from small boundary flow drainage through the nano-HBs that increases vesicle–surface interactions and the accessible binding surface area, while preserving the herringbone’s ability to enhance flow mixing in microchannels. Our data suggest that our nano-HB chip offers better exosome detection sensitivity than the existing methods<sup>3,8</sup>, including a nano-plasmonic sensor that requires at least 3,000 exosomes per assay<sup>4</sup>.

The nano-HB chip-based assay was then adapted to detect exosomes derived by ovarian cancer cell lines. We confirmed CD81 as the target for exosome immunocapture as it outperformed two commonly targeted exosomal markers—CD63 and CD9—when tested with the OVCAR3 exosomes (Supplementary Fig. 11a). CD81 was also found to be abundantly expressed in the ovarian cancer patient-derived exosomes in our previous studies<sup>8,39</sup>. We further verified the specificity of the anti-CD81 capture antibody for targeted immunodetection of ovarian cancer exosomes against

free proteins (Supplementary Fig. 11b). The nano-HB assay was then assessed for quantitative profiling of ovarian cancer-derived exosome subpopulations defined by six surface proteins (that is, human epidermal growth factor receptor 2, FRα, CA125, EpCAM, epidermal growth factor receptor and CD24). The presence of these biomarkers and high abundance of CD81 in ultracentrifugation-purified SKOV3 and OVCAR3 exosomes was verified by western blot (Fig. 4c). Using the nano-HB assay and a commercial exosome ELISA kit, the levels of the individual exosomal markers were quantified and normalized against CD24, which was found to be most abundant. The exosomal protein patterns obtained by the on-chip fluorescence detection for each cell line showed high similarity with those by the microplate chromogenic ELISA (Fig. 4d) and agreed well with the previously reported results<sup>4</sup>. Regression analysis of all measured values for six markers in both SKOV3 and OVCAR3 exosomes resulted in a strong linear correlation between the two methods (Pearson’s  $r=0.971$ ), validating the nano-HB ELISA detection for quantitative exosome analysis (Fig. 4e).

Lastly, we optimized the nano-HB assay for analysing clinical plasma samples. Specific detection of tumour-derived exosomes was assessed by probing the FRα<sup>+</sup> subtype in the purified SKOV3 EVs spiked in both PBS and a healthy plasma with no detectable FRα<sup>+</sup> exosomes (Fig. 4f). Analysis of spiked plasma demonstrated comparable analytical merits to those of spiked PBS, such as calibration sensitivity (that is, the slope: 0.1548 versus 0.1577) and LOD ( $1.0 \times 10^3$  versus  $0.9 \times 10^3$  total EVs  $\mu\text{l}^{-1}$ ). Such matched detection performance verifies that our optimized assay effectively reduces the matrix effects while maintaining high exosome binding efficiency. The LOD for the FRα<sup>+</sup> subtype ( $10^3$  total EVs  $\mu\text{l}^{-1}$ ) is in line with that for total exosomes ( $10 \mu\text{l}^{-1}$ ; Fig. 4b) because FRα<sup>+</sup> exosomes were found to account for a small fraction of total SKOV3 exosomes based on the measured relative FRα mRNA level (2.7% of GAPDH). Such high sensitivity allowed us to detect a low level of FRα<sup>+</sup> exosomes directly in 2  $\mu\text{l}$  ovarian cancer patient plasma, as verified by the measurements of a PBS blank and a control plasma ( $P < 0.001$ ; Fig. 4g). In contrast, the conventional flat-channel chip failed to detect such low-level FRα<sup>+</sup> exosomes in the same sample under the same assay conditions. Profiling of circulating exosomes directly from healthy and ovarian cancer plasma samples was also shown (Fig. 4h), identifying different biomarker profiles between the ovarian cancer cell lines (Fig. 4d) and the plasma, and among the patients and the control. It is noted that some tumour-relevant exosomes, such as the FRα<sup>+</sup> subtype, have quite low abundance despite a high level of total exosomes in the plasma. This can be attributed to small fractions of those subtypes in the overall exosomes derived by tumour cells, which are further reduced in patient biofluids by exosomes originated from non-cancer cells.

Accurate quantification of the fraction of a tumour-derived subtype in circulating exosomes is challenging. One of the challenges is that the molecular properties of tumour-associated exosomes are poorly understood, so the exosome number cannot be directly derived from quantifying their molecular contents<sup>40</sup>. Here, we implemented a simple strategy to estimate the fraction of tumour-associated subtypes in circulating exosomes (Supplementary Fig. 14). Briefly, a series of exosome standards of known quantities are assayed to quantify the total exosomes with anti-CD81 capture monoclonal antibodies and a mix of anti-CD9 and CD63 monoclonal antibodies for detection. The calibration plot establishes the correlation between exosome number and the measured level of CD9 and CD63. We assume that anti-CD81 captures all exosomes and that CD9 and CD63 combined can also detect all the captured exosomes and are evenly distributed on every vesicle. Based on this assumption, the subtype exosomes can be captured by specific monoclonal antibodies and quantified by measuring their CD9 and CD63 level to calculate the exosome number from the calibration plot. Using this approach, we estimated the fraction of FRα<sup>+</sup>

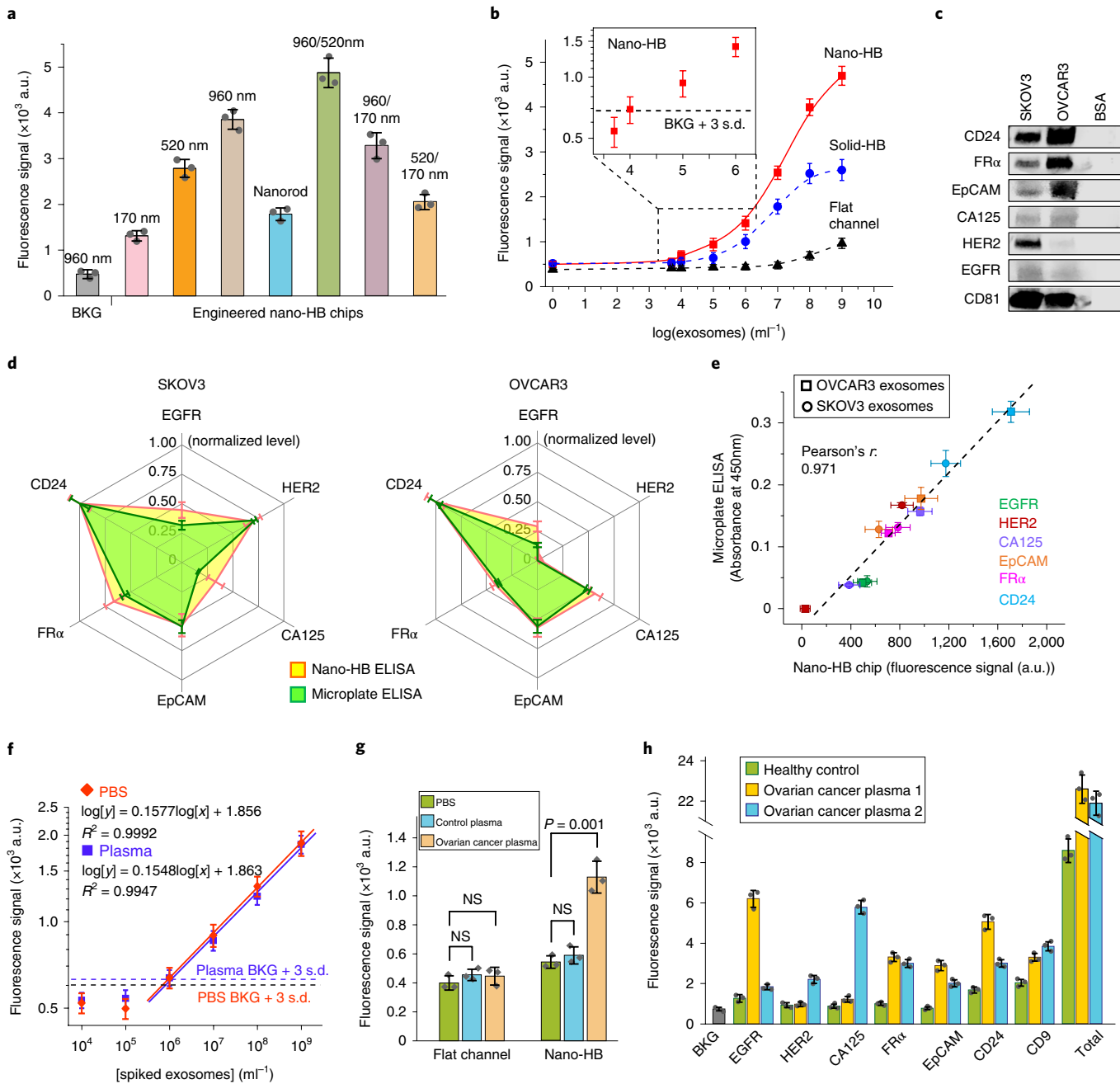


**Fig. 4 | Ultrasensitive detection of exosomes with the nano-HB chip.** **a**, Engineering nano-HBs using MINDS programmes the sensitivity for detecting COLO-1 exosomes ( $10^5 \mu\text{l}^{-1}$ ). Statistic comparison between the 960 and 960/520 nm chips yielded  $P=0.005$ . BKG, background. **b**, Calibration curves for quantifying total exosomes by the flat-channel, solid-HB and nano-HB chips. Serial tenfold-diluted COLO-1 exosome standards were used with a mixture of anti-CD9, CD63 and EpCAM monoclonal antibodies for detection. **c**, Western blot analysis of the protein markers in SKOV3 and OVCAR3 EVs with 10  $\mu\text{g}$  BSA as a negative control. **d**, Comparison of the nano-HB chip and a standard microplate kit for ELISA detection of six proteins in SKOV3 and OVCAR3 exosomes. For the nano-HB assay and microplate ELISA, respectively, 20  $\mu\text{l}$  purified EVs at  $10^5 \mu\text{l}^{-1}$  and 100  $\mu\text{l}$  EVs at  $10^6 \mu\text{l}^{-1}$  were used. All analyses were normalized against CD24, which was found to be most abundant. **e**, Measurements of six targets in SKOV3 and OVCAR3 exosomes by the nano-HB chip and microplate-based ELISA correlated well. **f**, Calibration curves for detecting the FR $\alpha^+$  subtype in ultracentrifugation-purified SKOV3 EVs spiked in PBS and a tenfold-diluted healthy plasma without detectable FR $\alpha$ . Total exosomes were captured with anti-CD81 monoclonal antibody and the FR $\alpha^+$  subtype was detected with anti-FR $\alpha$  monoclonal antibody. **g**, High sensitivity of the nano-HB chip enables the detection of FR $\alpha^+$  exosomes in an ovarian cancer plasma sample that are indiscernible using the conventional flat-channel chip. A two-tailed Student's *t*-test was used at a significance level of  $P<0.05$ . NS, not significant. **h**, Protein profiling of exosomes directly in plasma from a control and two ovarian cancer patients using nano-HB chips. Total exosomes were detected with a mix of CD9, CD63 and CD81 antibodies. The CD81 monoclonal antibody was used for exosome capture in all cases. Error bars represent 1 s.d. ( $n=3$ ).

exosomes to be  $4.5 \pm 0.8\%$  for patient 8, with a plasma exosome level of  $6.4 \times 10^{10} \text{ ml}^{-1}$  (Supplementary Fig. 14). This value agrees closely with that estimated by the exosomal expression of FR $\alpha$  mRNA rela-

tive to GAPDH (2.7%; Fig. 3h) if we assume that FR $\alpha$  mRNAs are homogeneously distributed in the tumour-associated exosomes with the same stoichiometry as GAPDH mRNAs across the whole

population. The accuracy of our method is limited by several key factors, such as the heterogeneous distribution of CD9 and CD63, inaccurate enumeration of total circulating exosomes by ultracentrifugation isolation and NTA, and lack of well-defined molecular properties of tumour exosomes. Nonetheless, our results suggest the level of clinically important exosomes; for example, those from early-stage tumours might be too low to be measured reliably with current capabilities, highlighting the necessity to develop ultrasensitive biosensing tools. Collectively, our studies suggest the superior sensitivity and clinical adaptability of our system, which could open new opportunities to advancing the clinical applications of exosomes.

#### Clinical analysis of circulating exosomes for cancer diagnosis.

As a proof of concept, we adapted the nano-HB system to assess circulating exosomes as a non-invasive tool for the diagnosis of ovarian cancer. We examined plasma samples collected from ovarian cancer patients ( $n=20$ ) and age-matched non-cancer controls ( $n=10$ ) (Supplementary Table 2). This sample size is sufficiently large to evaluate diagnostic accuracy with desired statistical errors (Supplementary Table 3)<sup>4,29</sup>. Our exosome profiling results show the universal presence of CD24 and EpCAM in exosomes from ovarian cancer cell lines and patient plasma, which is consistent with previous studies<sup>4,39</sup>. FR $\alpha$  is a promising target for cancer diagnosis and treatment<sup>41–43</sup>. However, FR $\alpha$  levels have been reported to be low in exosomes isolated from ovarian cancer cell lines<sup>4</sup> and have not yet been studied in circulating exosomes for ovarian cancer diagnosis. Interestingly, our method detected relatively abundant exosomal FR $\alpha$  in the ovarian cancer cell lines and plasma samples (Fig. 4). Thus, FR $\alpha$ , CD24 and EpCAM were further investigated as candidate biomarkers. Fig. 5a shows that CD24 and EpCAM were not only detected at high concentrations in ovarian cancer exosomes, but also in control samples. In contrast, FR $\alpha$  levels were much lower in ovarian cancer exosomes but importantly almost undetectable in control samples. We calibrated the nano-HB chip for protein immunoassay, which yielded a very low LOD for CD24 (100 fg ml<sup>-1</sup>), EpCAM (10 fg ml<sup>-1</sup>) and FR $\alpha$  (10 fg ml<sup>-1</sup>), respectively (Supplementary Fig. 15). The calibration curves were used to convert the fluorescence signals to protein concentrations. Despite the large interpatient heterogeneity observed, the levels of 3 markers can be used to discriminate the ovarian cancer patients from the controls (Supplementary Fig. 16;  $P=1 \times 10^{-12}$  for CD24;  $P=2 \times 10^{-10}$  for EpCAM and FR $\alpha$ , two-tailed Student's *t*-test).

The diagnostic performance of the nano-HB assay was systematically cross-validated by several gold standard methods. EVs were isolated from 2–3 ml plasma samples (Supplementary Table 2) following the established ultracentrifugation protocols<sup>31</sup>. A major size distribution of ~65–230 nm was determined for the purified EVs by NTA, with a shoulder peak probably due to the aggregated vesicles. SEM demonstrates the characteristic round-cup morphology (Supplementary Fig. 17a). Western blot analysis confirmed high expression of exosomal CD81 in ovarian cancer patients of various stages and detected a low level of FR $\alpha$  only in the stage IV patient (Supplementary Fig. 17b). The EV particle number by NTA and the total EV protein by Bradford assay were compared between the ovarian cancer patients and the controls, resulting in *P* values of 0.13 and 0.001, respectively (two-tailed Student's *t*-test; Supplementary Fig. 18). Thus, targeted analysis of tumour-associated exosomes by the nano-HB chip offers better diagnostic performance than these commonly applied approaches.

A subset of the plasma samples (ten ovarian cancer patients and five controls) was analysed by the combined assay of nano-HB capture and ddPCR and the microplate chromogenic ELISA kit to validate the nano-HB assay. The standard measurements of three exosomal markers at both mRNA and protein levels revealed similar expression patterns with the nano-HB assays, especially for the

patients with relatively high marker levels (Fig. 5b). Statistical analysis yielded a reasonably strong correlation between the nano-HB data and those of the ddPCR (Pearson's  $r=0.806$ ) and microplate ELISA (Pearson's  $r=0.831$ ). For both comparisons, a better linear correlation was observed for the high-concentration measurements and the reduced signal ratio at low concentrations, suggesting greater sensitivity of our method for clinical analysis of plasma exosomes (Supplementary Fig. 19). Moreover, compared with two standard methods, the nano-HB ELISA assay profoundly improved the detection of ovarian cancer cases (Supplementary Fig. 20) while demanding only a fraction of the sample volume (one-fifth) and assay time (around one-tenth). For instance, while 100  $\mu$ l plasma from each patient was processed for exosomal mRNA analysis, FR $\alpha$  transcripts were not detected in 4 out of 10 ovarian cancer patients (Supplementary Figs. 20 and 21). To test whether circulating exosomes reflect the molecular profiles of ovarian cancer tumour origin, we conducted immunofluorescence histological studies of three patient-matched tumour tissues (Supplementary Table 2) and observed relatively high expression of three markers (Fig. 5c and Supplementary Fig. 22). The expression of three markers in these patients' tissues was further verified by standard haematoxylin and eosin staining and immunohistochemistry analysis (Supplementary Fig. 23). The histological results suggest a correlation between the biomarker profiles of circulating exosomes and solid tumours, supporting potential applications of circulating exosomes as a non-invasive surrogate biopsy for tumours. Taken together, our validation studies corroborate the advantages of our technology for the highly sensitive and specific analysis of tumour-derived circulating exosomes with minimal sample consumption. Such analytical performance is particularly compelling for the development of non-invasive tools for preclinical screening and the early-stage diagnosis of cancer.

Statistical analyses of the nano-HB assay data in Fig. 5a were performed to quantitatively evaluate the diagnostic metrics of these exosomal markers. Analyses with receiver operating characteristic (ROC) curves revealed superior diagnostic accuracy for exosome profiling over NTA counting, with the areas under the curve (AUCs) for CD24, EpCAM, FR $\alpha$ , total protein, the three-marker set and exosome counts determined to be 1.00, 1.00, 0.995, 1.00, 1.00 and 0.709, respectively (Supplementary Fig. 24). The probing of exosomal CD24 and EpCAM has been documented for ovarian cancer diagnosis with high accuracy<sup>4,39</sup>. While exosomal FR $\alpha$  showed slightly less diagnostic power than CD24 and EpCAM due to its lower expression, it was almost undetectable in non-cancer controls, indicating its good tumour specificity. We assessed the nano-HB assays of three exosomal markers for detecting the control, early-stage (stage I/II) and advanced-stage ovarian cancer groups (stage III/IV) using one-way analysis of variance (ANOVA) with post-hoc Tukey's test. As summarized in Supplementary Table 4, ANOVA detected an overall significant difference among the three groups. Tukey's multiple comparison tests between the groups revealed that exosomal FR $\alpha$  could significantly differentiate the early-stage ovarian cancer from the advanced disease ( $P<0.002$ ), while CD24 ( $P=0.06$ ) and EpCAM ( $P=0.23$ ) could not (Fig. 5d and Supplementary Table 4). Recent studies revealed that the level of free FR $\alpha$  in the serum and plasma was very low in normal and benign conditions and significantly elevated in malignant ovarian tumours, with strong correlation with disease histotype, stage and grade<sup>42,43</sup>. Our results, albeit in a limited sample size, should support the clinical relevance of FR $\alpha$ , and suggest exosomal FR $\alpha$  as a potential marker for early ovarian cancer detection that warrants further investigation. To assess the feasibility of our technology for multiplexed exosome profiling to identify disease fingerprints, we performed non-supervised hierarchical clustering analysis of the measured levels of three exosomal tumour markers (Fig. 5e). The resultant heat map showed that the patients and controls were completely classified into distinct

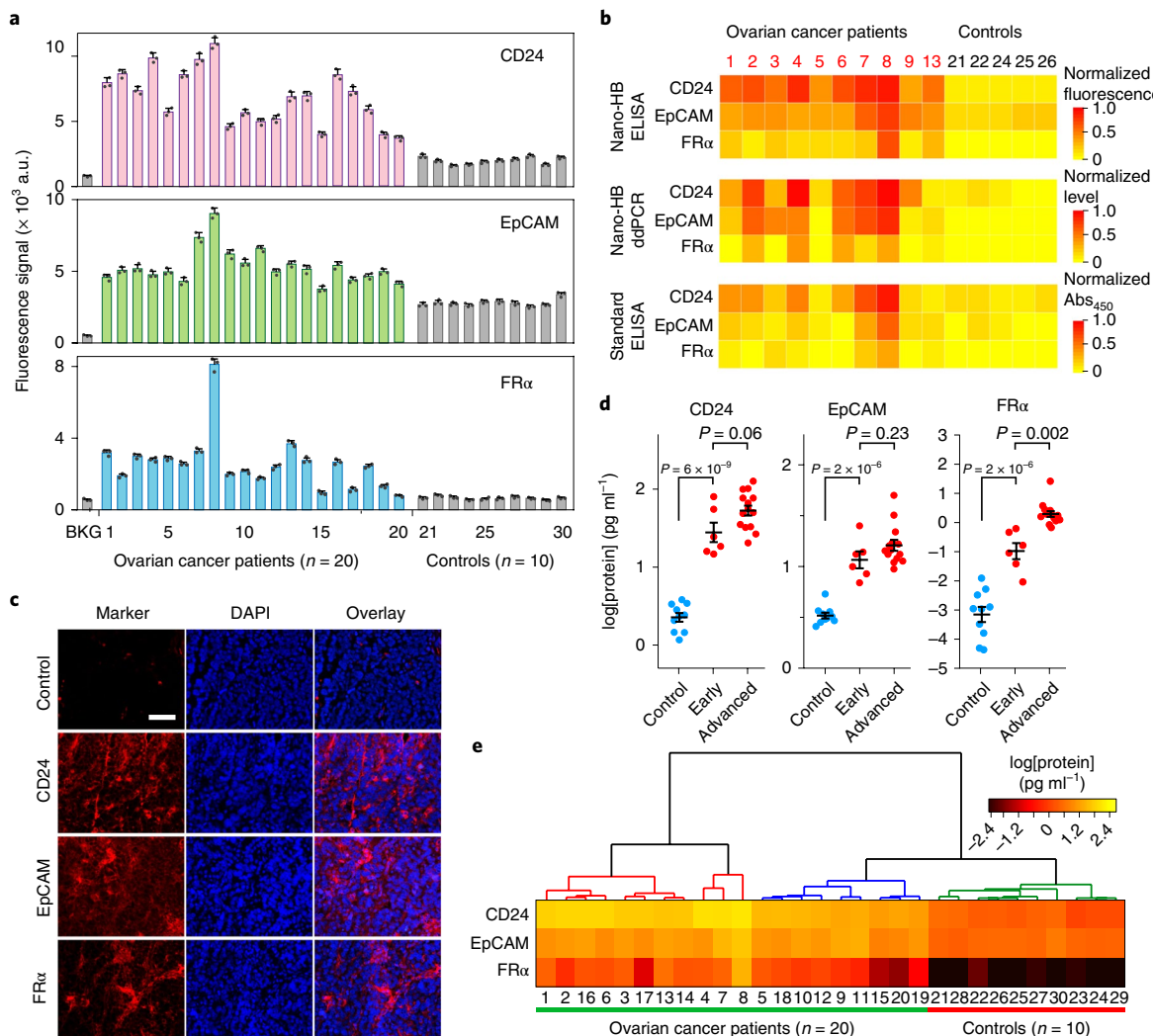


**Fig. 5 | Clinical profiling of circulating exosomes for the diagnosis of ovarian cancer.** **a**, Quantification of the exosomal levels of CD24, EpCAM and FR $\alpha$  proteins directly from the plasma of ovarian cancer patients ( $n=20$ ) and non-cancer controls ( $n=10$ ). Signals were subtracted by the corresponding background, measured with PBS, to determine the protein levels. Error bars indicate s.d. ( $n=3$ ). **b**, Comparison of exosomal marker patterns measured with the nano-HB ELISA, microplate ELISA, and combined nano-HB capture and ddPCR of mRNAs. A subset of ovarian cancer ( $n=10$ ) and control samples ( $n=5$ ) from **a** was assayed in triplicate, and the mean values were normalized against CD24 in patient 8 (the results with the highest levels). For mRNA analysis, 100  $\mu$ l plasma from each patient was diluted tenfold and run through 2 8-channel nano-HB chips to ensure fast and efficient exosome capture. **c**, Typical images of immunofluorescence histological assays of patient-matched tumour tissues (patient 11). Scale bar, 50  $\mu$ m. DAPI, 4',6-diamidino-2-phenylindole. **d**, Scatter dot plots of the plasma levels of three exosomal markers measured by nano-HB assay for patients of variable stages: control, early-stage (stage I/II) and advanced patients (stage III/IV). Error bars show means  $\pm$  1 s.e.m. Statistical comparison of three groups was performed by one-way ANOVA with post-hoc Tukey's test. The significance level was set at  $P < 0.05$ . **e**, A heat map constructed by non-supervised hierarchical clustering of the levels of exosomal CD24, EpCAM and FR $\alpha$  recognizes the ovarian cancer and control groups. Clustering analysis was performed with Ward linkage and Euclidean distance.

clusters by this three-marker combination, suggesting the potential of exosome profiling for ovarian cancer diagnosis and stratification. However, clinical promise of these biomarkers needs rigorous validation with much larger cohorts.

## Discussion

Microfluidic integration of nanostructures attracts enormous interest as it combines advantageous micro- and nanoscale phenomena to immensely improve biosensing<sup>44,45</sup>. However, device-scale microfluidic integration of 3D complex nanostructures has been a long-standing challenge. Standard nanofabrication techniques have mainly been used for small-scale 2D nanopatterning on planar surfaces. Existing 3D micro- and nanofabrication techniques, such as proximity field nanopatterning<sup>46</sup>, multibeam holographic lithography<sup>47</sup> and femtosecond laser printing<sup>48</sup>, require expensive, sophisticated facilities and labour-intensive, time-consuming fabrication procedures, severely limiting their scalability and practicality for routine applications. Nanoengineering of microfluidic sensing devices mostly involves surface modification of microfabricated elements with nanomaterials, yielding essentially 2D nanostructured sensing surfaces<sup>12,32,45,49</sup>. Alternatively, CSA enables simple, cost-effective fabrication of 3D nanomaterials with complex morphologies and has been applied extensively to material synthesis and photonics<sup>44,50</sup>. However, its bioanalytical applications remain largely underexplored. The MINDS strategy presents an enabling approach for developing new microfluidic nanosensing technologies. Compared with standard nanolithography, this bottom-up method affords several advantages: (1) simple

graphic lithography<sup>47</sup> and femtosecond laser printing<sup>48</sup>, require expensive, sophisticated facilities and labour-intensive, time-consuming fabrication procedures, severely limiting their scalability and practicality for routine applications. Nanoengineering of microfluidic sensing devices mostly involves surface modification of microfabricated elements with nanomaterials, yielding essentially 2D nanostructured sensing surfaces<sup>12,32,45,49</sup>. Alternatively, CSA enables simple, cost-effective fabrication of 3D nanomaterials with complex morphologies and has been applied extensively to material synthesis and photonics<sup>44,50</sup>. However, its bioanalytical applications remain largely underexplored. The MINDS strategy presents an enabling approach for developing new microfluidic nanosensing technologies. Compared with standard nanolithography, this bottom-up method affords several advantages: (1) simple

and programmable 3D assembly of complex nanostructures; (2) inherent compatibility with standard soft lithography for designed assembly and integration of device-scale nanostructures; and (3) broad applicability for nanobiosensing because it combines flexible and scalable microfluidic engineering with a wide spectrum of available nanomaterials<sup>44</sup>.

The probing of circulating exosomes has attracted rapidly increasing interest in clinical care, especially for non-invasive diagnosis and the monitoring of patient responses to treatment. Efficient isolation and specific measurement of disease-associated exosomes often present in low concentrations in biofluids remains challenging for conventional technologies. While microfluidics provides a uniquely suitable technology with which to surmount these challenges, existing microfluidic technologies have yielded limited improvements in exosome analysis<sup>3,8</sup>. In contrast with these techniques, the MINDS approach provides a simple yet powerful multiscale engineering strategy to simultaneously address the fundamental limits in mass transfer, reaction characteristics and boundary effects. We have shown that 3D nanoengineering of a herringbone mixer by the MINDS approach preserves the herringbone's performance in enhancing mass transfer, reduces the boundary flow resistance to promote surface-exosome interactions, and immensely increases the surface area for binding (Fig. 2). These distinct advantages result in an ultrasensitive system that permits rapid and specific immuno-sensing of tumour-related exosomes (for example, FR $\alpha^+$  exosomes) that present at undetectable concentrations in biological samples for conventional methods. We have shown that our technology can be adapted to exosome profiling in various cancer types, providing an enabling tool to facilitate studies of the biological functions and clinical relevance of exosomes.

Ovarian cancer is the fifth leading cause of cancer-related death among women in the United States. It is most commonly diagnosed at a late clinical stage (85% of patients), with a 5-year survival rate for patients of ~20%<sup>51</sup>. Currently, there is no single method capable of detecting ovarian cancer with high sensitivity and specificity, including CA125—the most commonly used ovarian tumour biomarker<sup>52</sup>. Tumour-derived exosomes in bodily fluids, such as ascites and blood, hold potential as diagnostic markers for non-invasive screening and early detection of cancer<sup>4,39</sup>. Relevant to future clinical applications, we have investigated alteration of CD24, EpCAM and FR $\alpha$  protein expression in ovarian cancer-associated exosomes to demonstrate the feasibility for non-invasive biomarker profiling of cancer (Fig. 5). FR $\alpha$  is a glycosylphosphatidylinositol-anchored protein that mediates folate transport into cells. Owing primarily to its largely restricted expression profile in normal tissues and upregulated expression in a variety of solid tumours, including serous ovarian cancer, FR $\alpha$  has recently been under intense investigation as a promising diagnostic and therapeutic target<sup>53</sup>. Despite its significant biological significance and clinical potential, the presence of FR $\alpha$  in exosomes has not yet received appreciable attention. Here, we have shown that our method could detect low levels of FR $\alpha$  in circulating exosomes from early-stage ovarian cancer patient plasma samples. The exosomal levels of FR $\alpha$  were significantly elevated in ovarian cancer, which could help in the detection of early-stage malignancies, supporting further investigations of the clinical potential of exosomal FR $\alpha$  as a blood biomarker for the sensitive and specific diagnosis of ovarian cancer. Overall, our proof-of-concept clinical analyses should validate the ability of our technology, not only for sensitive quantification of total circulating exosomes, but also exosome profiling to identify potential disease fingerprints for non-invasive ovarian cancer diagnosis and stratification. In principle, our nano-HB chip is applicable to a broad spectrum of targets of biomedical significance, including CTCs<sup>20,21,26</sup>. Therefore, our method provides a useful tool to facilitate the development of new biosensing technologies and clinical biomarkers.

## Methods

**Reagents and materials.** Monodispersed silica colloids were ordered from Bangs Laboratories. 3-MPS, 4-maleimidobutyric acid N-hydroxysuccinimide ester (GMBS), polyvinylpyrrolidone (PVP; molecular weight: ~40,000), anhydrous ethanol, 1-pentanol ( $\geq$ 99%) and sodium citrate dihydrate (99%) were purchased from Sigma–Aldrich. Ammonia (28%) and tetraethyl orthosilicate (98%) were obtained from Thermo Fisher Scientific. The ELISA kits for EpCAM, CD24 and FR $\alpha$  were ordered from R&D Systems. Streptavidin-conjugated  $\beta$ -galactosidase (S $\beta$ G), fluorescein-di- $\beta$ -D-galactopyranoside (FDG), DiO lipophilic dye, Vybrant CM-DiO cell staining solution and fluorescent nanoparticles (5% solid; excitation/emission wavelength: 540/560 nm; actual size: 46 nm) were purchased from Life Technologies. Detailed information on the antibodies used in our studies is listed in Supplementary Table 1. 1× PBS solution and SuperBlock buffer were from Mediatech and Thermo Fisher Scientific, respectively. All other solutions were prepared with deionized water (18.2 MV·cm; Thermo Fisher Scientific). S $\beta$ G and FDG were dissolved in PBS working solution (PBSW) at pH 7.4, which contains 0.5 mM DL-Dithiothreitol (Sigma–Aldrich), 2 mM MgCl<sub>2</sub> (Fluka Analytical) and 5% BSA (Sigma–Aldrich).

**Microfabrication of polydimethylsiloxane (PDMS) chips.** The MINDS approach uses a patterning chip for microfluidic CSA and an assay chip for exosome analysis, both of which are made of PDMS (Fig. 1b). The PDMS chips were fabricated using standard photolithography, as detailed previously<sup>8</sup>. All silicon moulds were patterned using SU-8 photoresist (MicroChem) following the procedures recommended by the manufacturer. For the patterning chips, we used SU-8 2010 to pattern the herringbone channel arrays with heights of 15, 25 and 35  $\mu$ m by controlling the spin-coating speed. For the assay chips, SU-8 2050 was employed to pattern the flow channels of 50  $\mu$ m in height. The prepared silicon moulds were pretreated with trichloro(1H,1H,2H,2H-perfluoroctyl) silane under vacuum for 4 h. Then, 33 g PDMS mixture at a base material:curing agent ratio of 10:1 was poured on the mould and cured in the oven at 70 °C for 4 h. PDMS slabs were peeled off from the moulds and the access holes were punched.

**Fabrication of nano-HB-integrated chips by MINDS.** The process of MINDS based on microfluidically guided CSA is schematically illustrated in Fig. 1b. Briefly, a PDMS patterning chip containing the herringbone channel array was sealed to clean glass slides without surface treatment. After 10 min sonication, 10  $\mu$ l of a 10% w/v aqueous suspension of monodisperse silica colloids was injected into the large solution reservoir shared by all channels. For co-assembly of colloids with different sizes, the total particle concentration of the mixed suspension was kept at 10% w/v. The colloidal solution spontaneously filled the microchannels and stopped at individual channel outlets, due to the surface tension. The solution reservoir was sealed with a small piece of PDMS such that solvent evaporation from the open reservoir induced CSA to fully pack the microchannels. Colloidal suspension in the reservoir was then replaced by 5% 3-MPS to strengthen the mechanical stability of the assembled colloidal structures. The packed device was then completely dried at 80 °C for 1 h on a hotplate. After carefully peeling off the patterning chip, the self-assembled herringbone structure was aligned and sealed with a UV-Ozone-treated PDMS assay layer under a stereoscope. The assay channel is 10 mm long, 2 mm wide and 50  $\mu$ m tall, containing 10 units of 5 herringbones.

**Synthesis of colloidal silica nanorods.** Monodisperse silica nanorods with a controlled aspect ratio were synthesized following a published wet-chemical method<sup>54</sup> with minor modifications. Briefly, a solution was prepared by completely dissolving 30 g PVP in 300 ml 1-pentanol. Then, 30 ml anhydrous ethanol, 8.4 ml ultrapure water, 2 ml 0.18 M aqueous solution of sodium citrate dihydrate, 6.75 ml fresh ammonia and 3 ml tetraethyl orthosilicate were sequentially added to the PVP solution with hand shaking. The well-mixed solution was left in the fumehood without stirring to let the reaction proceed at room temperature for ~4 h. The reaction mixture was then transferred into 50 ml centrifuge tubes. Monodisperse silica nanorods were purified by sequential centrifugation and washing: centrifugation at 2,000g for 1 h and re-dispersal of the sediment in ethanol, repeated at 1,500g for 15 min with ethanol (3 times) and water (3 times), and finally 4 times at 700g for 15 min and dispersal of the purified nanorods in ~40 ml water. Using transmission electron microscopy, the nanorods were determined to have an average diameter of  $238 \pm 32$  nm and length of  $1.34 \pm 0.26$   $\mu$ m (Supplementary Fig. 2).

**SEM characterization of nano-HB chips.** SEM images were taken using an FEI Versa 3D Dual Beam SEM at the University of Kansas Microscopy and Analytical Imaging Laboratory. To visualize exosomes captured on the surfaces, the samples were treated with 2.5% glutaraldehyde in PBS for 30 min, then rinsed for 3  $\times$  5 min to fix the exosomes. The samples were post-fixed for 15 min in 1% osmium tetroxide and rinsed for 10 min with water. The samples were dehydrated in a graded series of ethanol (30, 50, 70, 95 and 100%) for 2  $\times$  10 min at each step. The dehydrated samples were coated with a gold thin film using a high-resolution ion beam coater and imaged by SEM.

**Confocal imaging characterization of nano-HB chips.** Confocal images were taken with an Olympus 3I Spinning Disk Confocal Epifluorescence TIRF inverted

microscope equipped with 405, 488, 561 and 642 nm solid-state lasers. A 20 $\times$  long working distance air lens objective was used. The laser intensity was 100% and the exposure time was 3,000 ms. Image stacks were taken at 1  $\mu$ m intervals along the z axis, which ranged from the bottom of the nano-HB structures to the top of the flow channel. The obtained image stacks were fitted into 3D view photography using SlideBook version 5.5.

**Numerical simulation.** A computational fluid dynamics simulation was conducted using ANSYS CFX R17.2 software to solve incompressible Newtonian fluid with Navier–Stokes equations through a finite volume approximation. Water properties and a diffusion rate of  $5 \times 10^{-11} \text{ m}^2 \text{s}^{-1}$  were used to model the flow mixing of the nanoparticles suspended in water<sup>55</sup>. A solid-HB mixer with identical dimensions to the experiments was modelled first, omitting the porous domain, as the ‘baseline’ design to characterize the mixing efficiency in nano-HBs. This model included a structured mesh utilizing swept prism elements, due to the slanted nature of the geometry. A mesh sensitivity analysis was conducted to ensure the results were independent of the discretization of the computational domain. A total of 4,078,302 elements were used to capture the mixing interface appropriately and model the complex flow pattern. The porous herringbone nanostructure was modelled by defining a mathematical porous domain within the channel. Inside this porous domain, a momentum loss model was used to represent the flow restriction mathematically, following Darcy’s law. For this simulation, a ‘superficial velocity’ formulation was used to represent the nanoporous media with an isotropic, linear loss coefficient applied (permeability). The linear losses represent viscous losses while quadratic losses represent inertial loss. A widely used permeability–porosity relation in the field of flow in porous media—the Carman–Kozeny equation—was used to calculate the permeability for random close-packed monodisperse particles of 960 nm with a porosity of 0.35 (refs. <sup>28,56</sup>), yielding a permeability (linear loss coefficient) of  $4.7 \times 10^{-15} \text{ m}^2$ . Since the flow is laminar with viscous forces dominating, the inertial losses were neglected. A mathematical model of the porous domain was defined to resolve the nanoscale structure while capturing the microscale flow pattern, with reasonable computational effort for this proof-of-concept study.

**Cells and culture conditions.** The human ovarian cancer cell lines SKOV3 and OVCAR3 were cultured in RPMI-1640 media with 10% (*v/v*) vesicle-depleted foetal bovine serum (FBS), recombinant insulin (7.5  $\mu\text{g ml}^{-1}$ ), penicillin (100  $\text{U ml}^{-1}$ ) and streptomycin (100  $\mu\text{g ml}^{-1}$ ) at 37 °C in a humidified atmosphere with 5% CO<sub>2</sub>. Vesicle-depleted FBS was prepared by centrifuging FBS for 18 h at 100,000*g*, then passing the supernatant through a 0.22  $\mu\text{m}$  filter. Cell lines were maintained between 40 and 80% confluence, during which time the conditioned media was collected and replaced every 24 h. The collected media was immediately centrifuged at 2,000*g* for 10 min to remove large cell debris, then stored at 4 °C until a sufficient volume was pooled for exosome isolation.

**EV isolation.** EVs were isolated by differential ultracentrifugation of approximately 300 ml of conditioned media for each cell line collected over a 1–2 week period. Pooled conditioned media was spun for 45 min at 10,000*g* to pellet large vesicles. The supernatant was then spun at 100,000*g* for 1 h to pellet EVs. The supernatant was carefully decanted to avoid disturbing the EV pellet until ~2 ml remained. The 2 ml samples from multiple tubes were pooled in a 13.5 ml polypropylene Quick-Seal centrifuge tube (Beckman Coulter), then spun at 100,000*g* for 1 h to pellet the washed EVs. The supernatant was quickly and carefully removed and the EV pellet was re-suspended in 100–200  $\mu\text{l}$  of cold 0.22- $\mu\text{m}$ -filtered PBS and stored in low-retention tubes at –80 °C. Isolated EVs were characterized with NTA using NanoSight LM10 to determine the size and concentrations. The protein concentration was measured using a Bradford protein assay (Bio-Rad).

**Exosome immunoassay using the nano-HB chip.** The nano-HB chip was surface functionalized with 3-MPS for antibody conjugation via maleimide reaction. Briefly, the chips were filled with 5% 3-MPS in anhydrous ethanol solution and reacted for 1 h at room temperature. Excess silane was washed away with 70% ethanol 3 times, and 0.28 mg  $\text{ml}^{-1}$  GMBS was injected into the chip to modify the surface for 0.5 h. After washing with PBS, 0.1 mg  $\text{ml}^{-1}$  anti-CD81 antibody was flowed through the chip to coat the surface for 1 h at room temperature. The chips were blocked with 5% BSA for 2 h and stored at 4 °C before the experiments.

The lyophilized standard EVs of the colon cancer COLO-1 cell line were purchased from HansaBioMed and reconstituted in water before use. EVs of ovarian cancer cell lines SKOV3 and OVCAR3 were isolated from cell culture media by ultracentrifugation, as described above. The stock solution was aliquoted and stored at –80 °C. We determined the concentration of the stock solution by NTA and freshly prepared the standards by spiking the stock solution into PBS at different concentrations.

To characterize the nano-HB chip for exosome sensing, ultracentrifugation-purified EVs of known concentrations were prepared by serial dilutions of the stock solution in 1 ml PBS or 100  $\mu\text{l}$  tenfold-diluted plasma. Then, 20  $\mu\text{l}$  of the solution was pumped through the chip at a flow rate of 0.5  $\mu\text{l min}^{-1}$  using a microsyringe pump. The channel was then washed with PBS at 1  $\mu\text{l min}^{-1}$  for 10 min, filled with a mixture of 3 biotinylated detection antibodies for CD63,

CD81 and EpCAM (20  $\mu\text{g ml}^{-1}$  each) for the detection of exosomes (0.5  $\mu\text{l min}^{-1}$ ; 30 min), then washed with 10  $\mu\text{l}$  SuperBlock buffer for 10 min. S $\beta$ G prepared in PBSW buffer (20 ng  $\text{ml}^{-1}$ ) was introduced at 0.5  $\mu\text{l min}^{-1}$  for 15 min as the reporter enzyme. Excess enzyme was washed away by another 10  $\mu\text{l}$  SuperBlock buffer, then FDG in PBSW (500  $\mu\text{M}$ ) was introduced and reacted for 0.5 h in the dark for fluorescence detection assisted by enzymatic signal amplification. Fluorescence images were taken using a Zeiss Axiovert A1 inverted fluorescence microscope equipped with a light-emitting diode excitation light source (Thorlabs). The digital images were processed and analysed using ImageJ (National Institutes of Health; <http://rsbweb.nih.gov/ij/>) to measure the fluorescence intensity.

**Exosome analysis using microplate ELISA.** An ExoTEST Ready to Use kit was purchased from HansaBioMed. Purified SKOV3 and OVCAR3 EVs (100  $\mu\text{l}$  at 10 $\mu\text{l}^{-1}$ ) were added to each well of a 96-well plate. The plate was sealed with parafilm and incubated at room temperature while shaking for 30 min, then transferred into a 4 °C fridge for overnight incubation (12 h). Then, 200  $\mu\text{l}$  of washing buffer was added into each well, mixed by shaking and discard by pouring out. The washing step was repeated three times. The same biotinylated detection antibody as in the chip analysis was diluted to 2  $\mu\text{g ml}^{-1}$ , and 100  $\mu\text{l}$  was added to the wells. The plate was sealed and incubated at room temperature while shaking for 20 min, then incubated for 2 h at 4 °C. The plate was washed as above 3 times, then 100  $\mu\text{l}$  1:5,000-diluted horseradish peroxidase-streptavidin conjugate was added, with shaking at room temperature for 15 min and incubation at 4 °C for 1 h. Excess enzyme was washed away with the washing buffer three times. Lastly, 100  $\mu\text{l}$  of chromogenic substrate solution was added to each well and incubated for 10 min at room temperature in the dark. The reactions were stopped by adding 100  $\mu\text{l}$  of stop solution. The absorbance was measured at 450 nm on a Cytaion 5 imaging reader (BioTek), with subtraction of the background measured with PBS.

**Quantitative calibration of standard proteins.** On-chip protein quantitative assay was carried out for CD24, EpCAM and FR $\alpha$ , respectively, using a DuoSet ELISA kit (R&D Systems; Supplementary Table 1) consisting of capture antibody, standard protein and detection antibody. The capture antibody (0.1 mg  $\text{ml}^{-1}$ ) was immobilized on the nano-HB chip via 3-MPS and GMBS modification, as described above. After blocking with 5% BSA for 1 h, 20  $\mu\text{l}$  of standard proteins in PBS was flowed through the nano-HB chip within 2 h. The non-captured proteins were washed away using PBS with Tween 20 (PBST) washing buffer (0.05% Tween 20 and 1% BSA in PBS). Then, 10  $\mu\text{l}$  of biotinylated detection antibody (20  $\mu\text{g ml}^{-1}$ ) was introduced to label the captured proteins. After washing with PBST, S $\beta$ G and FDG were added in PBSW solution to trigger the enzymatic fluorescence amplification reaction. The fluorescence signal was measured as described above and plotted as a function of the protein concentration.

**Western blot analysis of EVs.** Western blotting was performed using 4–12% precast polyacrylamide slab mini-gels (Tris-glycine pH 8.3) in a Mini Trans-Blot module (Bio-Rad), following the standard protocol. Some 30–50  $\mu\text{g}$  purified EVs were pretreated with radioimmunoprecipitation assay lysis buffer with protease inhibitors on ice for at least 3 h and heated at 72 °C for 10 min after adding an equal volume of 2 $\times$  loading buffer. Electrophoresis was carried out at 125 V for 2 h, then the gels were electrotransferred to the cellulose membranes (0.2  $\mu\text{m}$ ) at 25 V for 2.5 h. The nitrocellulose membrane was first blocked with Odyssey Blocking Buffer (PBS), then incubated overnight at 4 °C in primary antibody (1:1,000). The membranes were washed 3 times for 10 min each (1x PBS and 0.5% Tween 20, pH 7.4), then immersed into goat anti-mouse IRDye 800CW secondary antibody (1:10,000) for 60 min at room temperature. Afterwards, the washing step was repeated three times. Imaging was performed using an Odyssey FC Imaging System (LI-COR Biosciences).

**mRNA analysis of ovarian cancer cell-derived EVs.** NTA counting reported a typical EV concentration of  $10^7$ – $10^8 \text{ ml}^{-1}$  in SKOV3 and OVCAR3 cell culture media, which is  $\sim 10^2$ – $10^4$ -fold lower than in human plasma. Because of the low concentration of EVs, hundreds of millilitres of the culture media were processed by ultracentrifugation to obtain the sufficient amount of vesicles for ddPCR analysis of six mRNA markers. For bulk analysis of ultracentrifugation-purified ovarian cancer EVs, total RNA was extracted from 40–60  $\mu\text{g}$  EVs using an RNAqueous-Micro Total RNA Isolation Kit (Ambion), then reverse transcribed to cDNA using a High-Capacity cDNA Reverse Transcription Kit (Applied Biosystems), per the manufacturer’s protocols. PCR mix was prepared by mixing 1  $\mu\text{l}$  of the obtained cDNA and commercial pre-designed primer sets for each mRNA target (PrimeTime qPCR Primer Assays; Integrated DNA Technologies) with QX200 ddPCR EvaGreen Supermix (Bio-Rad), following the manufacturer’s recommendations. ddPCR was performed using a QX200 Droplet Digital PCR System (Bio-Rad). The PCR protocol was 5 min at 95 °C, 30 s at 95 °C and 1 min at 55 °C for 40 cycles, then 5 min at 4 °C and 5 min at 90 °C. The background signal was determined for each assay and subtracted in the data analysis to eliminate non-specific amplification. Measurements of each mRNA target were repeated at least three times with different batches of purified EVs. The concentrations of target mRNAs were normalized against GAPDH.

The nano-HB chip is designed for diagnostic exosome analysis using non-invasive sample volumes, which can run 20–100 µl sample with a reasonable processing time (40–200 min). Chip isolation of exosomes from such a small volume of cell culture medium was found not to yield sufficient amounts of exosomes to detect the low-frequency mRNA targets by ddPCR. Based on the bulk mRNA analysis of ultracentrifugation-isolated EVs, it was estimated that at least 10 ml culture media is needed for nano-HB chip isolation and subsequent ddPCR analysis of the mRNA targets, which is beyond the sample processing capacity of the chip. Therefore, we used the ultracentrifugation-concentrated SKOV3 and OVCAR3 EVs to characterize the nano-HB capture for mRNA profiling of exosomes. To this end, 100 µl of the concentrated EVs ( $10^6 \mu\text{l}^{-1}$ ) was run on the chip modified with anti-CD81 capture antibody with protein G as the linker<sup>1</sup>. Captured exosomes were eluted out by flowing 20 µl Pierce IgG Elution Buffer (Thermo Fisher Scientific) through the chip, which will dissociate capture antibodies from Protein G. We lysed the eluted exosomes, extracted total RNA and performed ddPCR analysis of the mRNA targets, as described above. The profiles of six mRNA markers measured in the chip-purified exosomes were compared with that of bulk analysis of ultracentrifugation-purified EVs.

**Clinical exosome ELISA analysis using nano-HB chips and the microplate kit.** De-identified plasma samples from ovarian cancer patients and cancer-free individuals were provided from the University of Kansas Cancer Center's Biospecimen Repository Core Facility (BRCF) along with accompanying clinical information (Supplementary Table 2). Blood specimens (that is, plasma samples) were obtained from individuals enrolled under the repository's Institutional Review Board-approved protocol (HSC 5929) and following US Common Rule. Once a patient provided written, informed consent in accordance with the BRCF's Institutional Review Board protocol, blood was collected by BRCF staff and processed for long-term storage at  $-80^\circ\text{C}$ . We estimated the required sample size for evaluating diagnostic accuracy by comparing the area under a ROC curve (AUC) with a null hypothesis value of 0.5. For conventional characterization of the samples, EVs were purified by ultracentrifugation, then characterized by NTA sizing, Bradford assay and Western blot, following the protocols we established<sup>31</sup>. For microfluidic analysis, 2 µl plasma was used without any pretreatment except 10× dilution with PBS to permit convenient injection using a 50 µl syringe and prevent channel clogging. Exosome assay and data acquisition followed the same processes as for exosome standards. We used the CD81 monoclonal antibody for capture, and specific monoclonal antibodies ( $20 \mu\text{g ml}^{-1}$ ) for immunodetection of CD24, EpCAM and FRα.

For analysis of plasma exosomes using the standard method, the ExoTEST Ready to Use kit from HansaBioMed was used. Ten ovarian cancer patients and five controls listed in Supplementary Table 2 were selected for standard microplate ELISA. Plasma samples (10 µl) were diluted tenfold to 100 µl and added to each well of a 96-well plate. The assays were carried out following the protocol described above.

**Clinical exosome mRNA analysis.** For mRNA analysis of exosomes in patient plasma, we expanded the nano-HB chip to an eight-channel device to enhance the capacity and throughput for exosome capture. Plasma (100 µl) from each patient was diluted tenfold and run through 2 8-channel chips for 2 h to capture sufficient exosomes for subsequent ddPCR assays. Elution of the captured exosomes by 20 µl Pierce IgG elution buffer, exosome lysis, total RNA extraction, cDNA synthesis and ddPCR assays was performed as described above.

**Histological analysis of patient-matched tissues.** The immunofluorescence histology analysis of patient-matched tissues was performed in the Histology Laboratory at the University of Kansas Medical Center following the standard protocol<sup>31</sup>. Briefly, the fresh frozen ovarian cancer tissues were embedded in optimal cutting temperature compound in cryomoulds and cut into 4-µm-thick cryostat sections. The slides were fixed in ice-cold acetone for 5 min and washed with PBST for 2 min after 30 min of air drying. Then, 1% BSA was used to block the tissue sections for 30 min. The same primary detection antibodies (1:100 dilution) as in the exosome immunoassay were added and incubated at  $4^\circ\text{C}$  overnight. After washing with PBST, 0.4 µM 4',6-diamidino-2-phenylindole in PBS and secondary detection antibody goat anti-mouse IgG (1:100 dilution; Cy5 labelled) were incubated sequentially with the tissue sections. After staining, the tissue sections were mounted on coverslips and imaged using an upright epifluorescence microscope (Nikon Eclipse 80i) equipped with a 20× or 40× objective and 3 colour filter sets (blue, green and red). Images were collected and merged in three-colour using MetaMorph, and analysed using ImageJ. Immunohistochemical staining was performed according to the following procedure. Paraffin sections of 4 µm were mounted on Fisherbrand Superfrost slides, baked for 60 min at  $60^\circ\text{C}$ , then deparaffinized. Epitope retrieval was performed using a BioCare Medical Decloaking Chamber (pressure cooker) under pressure for 5 min, using pH 6.0 Citrate Buffer followed by a 10 min cool-down period. Endogenous peroxidase was blocked with 3% H<sub>2</sub>O<sub>2</sub> for 10 min followed by incubation with a specific primary antibody for 30 min: a 1:100 dilution of monoclonal EpCAM (MOC-31; Abcam); a 1:50 dilution of monoclonal CD24 (SN3; Thermo Fisher Scientific); ready-to-use monoclonal FOLR1 (26B3.F2;

Biocare Medical); and ready-to-use monoclonal p53 (DO-7; Dako). This was followed by EnVision+ anti-mouse secondary antibody (Dako) for 30 min and DAB+ Chromogen (Dako) for 5 min. Immunohistochemical staining was performed using an IntelliPATH FLX automated stainer at room temperature. A light haematoxylin counterstain was performed, following which the slides were dehydrated, cleared and mounted using permanent mounting media.

**Statistical analysis.** We estimated the required sample size for ROC analysis of diagnostic accuracy by comparing the area under a ROC curve (AUC) with a null hypothesis value of 0.5. Statistical calculation was performed at various type I error  $\alpha$  and type II error  $\beta$  levels with an expected AUC of 0.8 and a sample allocation ratio of 0.5 (control/patient). The computed sample sizes are listed in Supplementary Table 3. A total sample size of 30 (that is, 10 non-cancer controls and 20 ovarian cancer patients) is sufficient for statistical evaluation of diagnostic accuracy.

To mitigate analytical variations, detection signals for biomarkers were corrected by the background measured in parallel. Each measurement was repeated at least three times. Mean, s.d. and s.e.m. values were calculated with standard formulas. To compare the patient and control groups, a two-tailed Student's *t*-test was performed with a significance level of  $P < 0.05$ . The overall statistical significance of difference in the mean levels of exosomal CD24, EpCAM and FRα among the control, early-stage (stage I/II) and advanced groups (stage III/IV) was tested using one-way ANOVA. The significance of difference between two groups was evaluated by post-hoc Tukey's test (Supplementary Table 4). An outlier in the FRα data was detected by Grubbs' test and excluded from the post-hoc test. Clustering and ROC curve analyses were performed using the protein levels of exosomal CD24, EpCAM and FRα in Fig. 5e and the NTA data in Supplementary Fig. 16, with the R package<sup>37</sup>. For the combined three-marker set, the arithmetic average of the levels of three markers was used as an independent variable for calculation. Non-supervised hierarchical clustering analysis was performed with Ward linkage and Euclidean distance to generate a heat map with the dendrogram. A 95% confidence level was used for all statistical analyses.

**Reporting Summary.** Further information on research design is available in the Nature Research Reporting Summary linked to this article.

## Data availability

The authors declare that all data supporting the findings of this study are available within the paper and its Supplementary Information files. The raw and analysed datasets generated during the study are available for research purposes from the corresponding author on reasonable request.

Received: 8 May 2017; Accepted: 16 January 2019;

Published online: 25 February 2019

## References

- Schwarzenbach, H., Nishida, N., Calin, G. A. & Pantel, K. Clinical relevance of circulating cell-free microRNAs in cancer. *Nat. Rev. Clin. Oncol.* **11**, 145–156 (2014).
- Haber, D. A. & Velculescu, V. E. Blood-based analyses of cancer: circulating tumor cells and circulating tumor DNA. *Cancer Discov.* **4**, 650–661 (2014).
- He, M. & Zeng, Y. Microfluidic exosome analysis toward liquid biopsy for cancer. *J. Lab. Autom.* **21**, 599–608 (2016).
- Im, H. et al. Label-free detection and molecular profiling of exosomes with a nano-plasmonic sensor. *Nat. Biotechnol.* **32**, 490–495 (2014).
- Yanez-Mo, M. et al. Biological properties of extracellular vesicles and their physiological functions. *J. Extracell. Vesicles* **4**, 27066 (2015).
- Atay, S. et al. Oncogenic KIT-containing exosomes increase gastrointestinal stromal tumor cell invasion. *Proc. Natl. Acad. Sci. USA* **111**, 711–716 (2014).
- Melo, S. A. et al. Glypican-1 identifies cancer exosomes and detects early pancreatic cancer. *Nature* **523**, 177–182 (2015).
- Zhang, P., He, M. & Zeng, Y. Ultrasensitive microfluidic analysis of circulating exosomes using a nanostructured graphene oxide/polydopamine coating. *Lab Chip* **16**, 3033–3042 (2016).
- Squires, T. M., Messinger, R. J. & Manalis, S. R. Making it stick: convection, reaction and diffusion in surface-based biosensors. *Nat. Biotechnol.* **26**, 417–426 (2008).
- Stroock, A. D. et al. Chaotic mixer for microchannels. *Science* **295**, 647–651 (2002).
- Shang, Y., Zeng, Y. & Zeng, Y. Integrated microfluidic lectin barcode platform for high-performance focused glycomic profiling. *Sci. Rep.* **6**, 20297 (2016).
- Kelley, S. O. et al. Advancing the speed, sensitivity and accuracy of biomolecular detection using multi-length-scale engineering. *Nat. Nanotechnol.* **9**, 969–980 (2014).
- Soleymani, L., Fang, Z., Sargent, E. H. & Kelley, S. O. Programming the detection limits of biosensors through controlled nanostructuring. *Nat. Nanotechnol.* **4**, 844–848 (2009).

14. Bin, X., Sargent, E. H. & Kelley, S. O. Nanostructuring of sensors determines the efficiency of biomolecular capture. *Anal. Chem.* **82**, 5928–5931 (2010).
15. Wang, S. et al. Three-dimensional nanostructured substrates toward efficient capture of circulating tumor cells. *Angew. Chem.* **48**, 8970–8973 (2009).
16. Chen, G. D., Fachin, F., Fernandez-Suarez, M., Wardle, B. L. & Toner, M. Nanoporous elements in microfluidics for multiscale manipulation of bioparticles. *Small.* **7**, 1061–1067 (2011).
17. Chen, G. D., Fachin, F., Colombini, E., Wardle, B. L. & Toner, M. Nanoporous micro-element arrays for particle interception in microfluidic cell separation. *Lab Chip* **12**, 3159–3167 (2012).
18. Fachin, F., Chen, G. D., Toner, M. & Wardle, B. L. Integration of bulk nanoporous elements in microfluidic devices with application to biomedical diagnostics. *J. Microelectromech. Syst.* **20**, 1428–1438 (2011).
19. Zeng, Y. & Harrison, D. J. Self-assembled colloidal arrays as three-dimensional nanofluidic sieves for separation of biomolecules on microchips. *Anal. Chem.* **79**, 2289–2295 (2007).
20. Stott, S. L. et al. Isolation of circulating tumor cells using a microvortex-generating herringbone-chip. *Proc. Natl Acad. Sci. USA* **107**, 18392–18397 (2010).
21. Wang, S. et al. Highly efficient capture of circulating tumor cells by using nanostructured silicon substrates with integrated chaotic micromixers. *Angew. Chem.* **50**, 3084–3088 (2011).
22. Singh, G., Pillai, S., Arpanaei, A. & Kingshott, P. Multicomponent colloidal crystals that are tunable over large areas. *Soft Matter* **7**, 3290–3294 (2011).
23. Nazemifar, N. et al. A systematic evaluation of the role of crystalline order in nanoporous materials on DNA separation. *Lab Chip* **12**, 146–152 (2012).
24. Adams, A. A. et al. Highly efficient circulating tumor cell isolation from whole blood and label-free enumeration using polymer-based microfluidics with an integrated conductivity sensor. *J. Am. Chem. Soc.* **130**, 8633–8641 (2008).
25. Forbes, T. P. & Kralj, J. G. Engineering and analysis of surface interactions in a microfluidic herringbone micromixer. *Lab Chip* **12**, 2634–2637 (2012).
26. Sheng, W. et al. Capture, release and culture of circulating tumor cells from pancreatic cancer patients using an enhanced mixing chip. *Lab Chip* **14**, 89–98 (2014).
27. Philipse, A. P. & Pathmamanoharan, C. Liquid permeation (and sedimentation) of dense colloidal hard-sphere packings. *J. Colloid. Interface Sci.* **159**, 96–107 (1993).
28. Frishfelds, V., Hellstrom, J. G. I. & Lundstrom, T. S. Flow-induced deformations within random packed beds of spheres. *Transport Porous Med.* **104**, 43–56 (2014).
29. Shao, H. et al. Chip-based analysis of exosomal mRNA mediating drug resistance in glioblastoma. *Nat. Commun.* **6**, 6999 (2015).
30. Kanwar, S. S., Dunlay, C. J., Simeone, D. M. & Nagrath, S. Microfluidic device (ExoChip) for on-chip isolation, quantification and characterization of circulating exosomes. *Lab Chip* **14**, 1891–1900 (2014).
31. He, M., Crow, J., Roth, M., Zeng, Y. & Godwin, A. K. Integrated immunoisolation and protein analysis of circulating exosomes using microfluidic technology. *Lab Chip* **14**, 3773–3780 (2014).
32. Reategui, E. et al. Engineered nanointerfaces for microfluidic isolation and molecular profiling of tumor-specific extracellular vesicles. *Nat. Commun.* **9**, 175 (2018).
33. Wan, Y. et al. Rapid magnetic isolation of extracellular vesicles via lipid-based nanoprobe. *Nat. Biomed. Eng.* **1**, 0058 (2017).
34. Lobb, R. J. et al. Optimized exosome isolation protocol for cell culture supernatant and human plasma. *J. Extracell. Vesicles* **4**, 27031 (2015).
35. Domcke, S., Sinha, R., Levine, D. A., Sander, C. & Schultz, N. Evaluating cell lines as tumour models by comparison of genomic profiles. *Nat. Commun.* **4**, 2126 (2013).
36. Skog, J. et al. Glioblastoma microvesicles transport RNA and proteins that promote tumour growth and provide diagnostic biomarkers. *Nat. Cell Biol.* **10**, 1470–1476 (2008).
37. Davies, R. T. et al. Microfluidic filtration system to isolate extracellular vesicles from blood. *Lab Chip* **12**, 5202–5210 (2012).
38. Li, S., Zhao, J., Lu, P. & Xie, Y. Maximum packing densities of basic 3D objects. *Chinese Sci. Bull.* **55**, 114–119 (2010).
39. Zhao, Z., Yang, Y., Zeng, Y. & He, M. A microfluidic ExoSearch chip for multiplexed exosome detection towards blood-based ovarian cancer diagnosis. *Lab Chip* **16**, 489–496 (2016).
40. Chevillet, J. R. et al. Quantitative and stoichiometric analysis of the microRNA content of exosomes. *Proc. Natl Acad. Sci. USA* **111**, 14888–14893 (2014).
41. Toffoli, G. et al. Overexpression of folate binding protein in ovarian cancers. *Int. J. Cancer* **74**, 193–198 (1997).
42. Kuroasaki, A. et al. Serum folate receptor alpha as a biomarker for ovarian cancer: implications for diagnosis, prognosis and predicting its local tumor expression. *Int. J. Cancer* **138**, 1994–2002 (2016).
43. Leung, F., Dimitrakakis, A., Kobayashi, H., Diamandis, E. P. & Kulasingam, V. Folate-receptor 1 (FOLR1) protein is elevated in the serum of ovarian cancer patients. *Clin. Biochem.* **46**, 1462–1468 (2013).
44. Yang, J., Choi, M. K., Kim, D. H. & Hyeon, T. Designed assembly and integration of colloidal nanocrystals for device applications. *Adv. Mater.* **28**, 1176–1207 (2016).
45. Kim, J., Li, Z. & Park, I. Direct synthesis and integration of functional nanostructures in microfluidic devices. *Lab Chip* **11**, 1946–1951 (2011).
46. Jeon, S., Malyarchuk, V., White, J. O. & Rogers, J. A. Optically fabricated three dimensional nanofluidic mixers for microfluidic devices. *Nano Lett.* **5**, 1351–1356 (2005).
47. Park, S. G., Lee, S. K., Moon, J. H. & Yang, S. M. Holographic fabrication of three-dimensional nanostructures for microfluidic passive mixing. *Lab Chip* **9**, 3144–3150 (2009).
48. Hu, Y. et al. Laser printing hierarchical structures with the aid of controlled capillary-driven self-assembly. *Proc. Natl Acad. Sci. USA* **112**, 6876–6881 (2015).
49. Cederquist, K. B. & Kelley, S. O. Nanostructured biomolecular detectors: pushing performance at the nanoscale. *Curr. Opin. Chem. Biol.* **16**, 415–421 (2012).
50. Vogel, N., Retsch, M., Fustin, C. A., Del Campo, A. & Jonas, U. Advances in colloidal assembly: the design of structure and hierarchy in two and three dimensions. *Chem. Rev.* **115**, 6265–6311 (2015).
51. Bast, R. C. Jr, Hennessy, B. & Mills, G. B. The biology of ovarian cancer: new opportunities for translation. *Nat. Rev. Cancer* **9**, 415–428 (2009).
52. Bodurka, D. C. et al. Reclassification of serous ovarian carcinoma by a 2-tier system: a Gynecologic Oncology Group study. *Cancer* **118**, 3087–3094 (2012).
53. Cheung, A. et al. Targeting folate receptor alpha for cancer treatment. *Oncotarget* **7**, 52553–52574 (2016).
54. Kuijk, A., van Blaaderen, A. & Imhof, A. Synthesis of monodisperse, rodlike silica colloids with tunable aspect ratio. *J. Am. Chem. Soc.* **133**, 2346–2349 (2011).
55. Kastelowitz, N. & Yin, H. Exosomes and microvesicles: identification and targeting by particle size and lipid chemical probes. *ChemBioChem* **15**, 923–928 (2014).
56. Müllner, T., Unger, K. K. & Tallarek, U. Characterization of microscopic disorder in reconstructed porous materials and assessment of mass transport-relevant structural descriptors. *New J. Chem.* **40**, 3993–4015 (2016).
57. Warnes, G. R. et al. gplots: Various R Programming Tools for Plotting Data v.3.0.1.1 (CRAN, 2019); <https://cran.r-project.org/web/packages/gplots/index.html>

## Acknowledgements

We thank the microfabrication core facility at the KU COBRE Center for Molecular Analysis of Disease Pathways for device fabrication, and the KU Cancer Center's Biospecimen Repository Core Facility, funded in part by the National Cancer Institute Cancer Center Support Grant (P30 CA168524) for providing clinical plasma samples, T. Meyer (KUMC) for technical support with immunohistochemistry, R. Madan (KUMC) for histopathology review, and H. Pathak (KUCC) for technical guidance with cell line-derived exosome isolations. This study was supported by 1R21CA186846, 1R21CA207816, 1R21EB024101, 1R33CA214333 and P20GM103638 from the NIH. P.Z. was supported by the postdoc award from the Kansas IDEAS Network of Biomedical Research Excellence under the grant P20GM103418 from NIH/NIGMS. A.K.G. is the Chancellors Distinguished Chair in Biomedical Sciences Endowed Professor.

## Author contributions

Y.Z. conceived and supervised the project. P.Z. and Y.Z. designed the research. P.Z. performed the technology development, microfluidic analysis and microscopic imaging. X.Z. and P.Z. conducted mRNA profiling. M.H. contributed to numerical simulation. Y.S. isolated exosomes from clinical samples, and conducted western blot and some NTA analyses. A.L.T. isolated exosomes from cell culture media and helped with the immunohistochemistry. A.K.G. provided clinical samples and assisted in clinical studies. P.Z., X.Z., M.H., Y.S., A.K.G. and Y.Z. analysed the data. P.Z. and Y.Z. wrote the manuscript. All authors edited the manuscript.

## Competing interests

The authors declare no competing interests.

## Additional information

**Supplementary information** is available for this paper at <https://doi.org/10.1038/s41551-019-0356-9>.

**Reprints and permissions information** is available at [www.nature.com/reprints](http://www.nature.com/reprints).

**Correspondence and requests for materials** should be addressed to Y.Z.

**Publisher's note:** Springer Nature remains neutral with regard to jurisdictional claims in published maps and institutional affiliations.

© The Author(s), under exclusive licence to Springer Nature Limited 2019

# Reporting Summary

Nature Research wishes to improve the reproducibility of the work that we publish. This form provides structure for consistency and transparency in reporting. For further information on Nature Research policies, see [Authors & Referees](#) and the [Editorial Policy Checklist](#).

## Statistical parameters

When statistical analyses are reported, confirm that the following items are present in the relevant location (e.g. figure legend, table legend, main text, or Methods section).

n/a Confirmed

- The exact sample size ( $n$ ) for each experimental group/condition, given as a discrete number and unit of measurement
- An indication of whether measurements were taken from distinct samples or whether the same sample was measured repeatedly
- The statistical test(s) used AND whether they are one- or two-sided  
*Only common tests should be described solely by name; describe more complex techniques in the Methods section.*
- A description of all covariates tested
- A description of any assumptions or corrections, such as tests of normality and adjustment for multiple comparisons
- A full description of the statistics including central tendency (e.g. means) or other basic estimates (e.g. regression coefficient) AND variation (e.g. standard deviation) or associated estimates of uncertainty (e.g. confidence intervals)
- For null hypothesis testing, the test statistic (e.g.  $F$ ,  $t$ ,  $r$ ) with confidence intervals, effect sizes, degrees of freedom and  $P$  value noted  
*Give P values as exact values whenever suitable.*
- For Bayesian analysis, information on the choice of priors and Markov chain Monte Carlo settings
- For hierarchical and complex designs, identification of the appropriate level for tests and full reporting of outcomes
- Estimates of effect sizes (e.g. Cohen's  $d$ , Pearson's  $r$ ), indicating how they were calculated
- Clearly defined error bars  
*State explicitly what error bars represent (e.g. SD, SE, CI)*

*Our web collection on [statistics for biologists](#) may be useful.*

## Software and code

Policy information about [availability of computer code](#)

Data collection

Zeiss Zen Lite Imaging Software 2012, ANSYS CFX R17.2 software, SlideBook version 5.5, BioTek Gen5 Microplate Reader and Imager Software, QuantaSoft ddPCR software, and LabVIEW 2016.

Data analysis

ImageJ, Excel 2016, QuantaSoft ddPCR software, Leica Application Suite X (LAS X), R, and Origin 2016.

For manuscripts utilizing custom algorithms or software that are central to the research but not yet described in published literature, software must be made available to editors/reviewers upon request. We strongly encourage code deposition in a community repository (e.g. GitHub). See the Nature Research [guidelines for submitting code & software](#) for further information.

## Data

Policy information about [availability of data](#)

All manuscripts must include a [data availability statement](#). This statement should provide the following information, where applicable:

- Accession codes, unique identifiers, or web links for publicly available datasets
- A list of figures that have associated raw data
- A description of any restrictions on data availability

The authors declare that all data supporting the findings of this study are available within the paper and its Supplementary Information. The raw and analysed datasets generated during the study are available for research purposes from the corresponding author on reasonable request.

# Field-specific reporting

Please select the best fit for your research. If you are not sure, read the appropriate sections before making your selection.

Life sciences       Behavioural & social sciences       Ecological, evolutionary & environmental sciences

For a reference copy of the document with all sections, see [nature.com/authors/policies/ReportingSummary-flat.pdf](https://nature.com/authors/policies/ReportingSummary-flat.pdf)

## Life sciences study design

All studies must disclose on these points even when the disclosure is negative.

Sample size	As a proof-of-concept, we examined plasma samples collected from OvCa patients ( $n = 20$ ) and age-matched non-cancer controls ( $n = 10$ ) (Supplementary Table S2). This sample size is sufficiently large to evaluate diagnostic accuracy with reasonable statistical errors (Table S3).
Data exclusions	No data were excluded from the analyses.
Replication	All the measurements were repeated for at least three times. Negative and positive controls were included to correct the measurement when relevant.
Randomization	Human plasma samples were randomly pulled out from the KU Cancer Center's Biospecimen Repository Core Facility (BRCF) and patients were randomly selected from an age range of 50-80 years old (Table S1).
Blinding	The study was not blinded.

## Reporting for specific materials, systems and methods

### Materials & experimental systems

n/a	Involved in the study
<input checked="" type="checkbox"/>	Unique biological materials
<input type="checkbox"/>	Antibodies
<input type="checkbox"/>	Eukaryotic cell lines
<input checked="" type="checkbox"/>	Palaeontology
<input checked="" type="checkbox"/>	Animals and other organisms
<input type="checkbox"/>	Human research participants

### Methods

n/a	Involved in the study
<input checked="" type="checkbox"/>	ChIP-seq
<input checked="" type="checkbox"/>	Flow cytometry
<input checked="" type="checkbox"/>	MRI-based neuroimaging

## Antibodies

### Antibodies used

All the antibodies used are provided in Table S1.

### Validation

The antibodies have all been validated by the manufacturers, and their specificity and cross-reactivity for the protein targets of interest have been also validated using either microplate ELISA, Western Blot, or on-chip ELISA.

## Eukaryotic cell lines

Policy information about [cell lines](#)

### Cell line source(s)

COLO-1 and MCF-7 cells were cultured and EVs were purified from the culture media by HansaBioMed, Inc. SKOV3 and OVCAR3 cell lines were obtained from ATCC and cultured in the lab of Dr. Godwin (co-author) at KUMC.

### Authentication

COLO-1 and MCF-7 cells were authenticated with Short Tandem Repeat (STR) profiling by the provider biobank (Interlab Cell Line Collection, Italy) for HansaBioMed, Inc. All the cell lines cultured in Dr Godwin's lab were authenticated by STR allele profiling and sequencing by an independent source (University of Arizona Genetics Core, Tucson, AZ –Cell line Authentication Core). All cell lines in Dr Godwin's lab are screened for mycoplasma contamination every 6 months.

### Mycoplasma contamination

Cell lines tested negative for mycoplasma contamination.

### Commonly misidentified lines (See [ICLAC](#) register)

No commonly misidentified cell lines were used.

## Human research participants

Policy information about [studies involving human research participants](#)

Population characteristics

Human plasma samples were obtained from the University of Kansas Cancer Center's Biospecimen Repository Core Facility under the protocol (IRB #5929) approved by the internal Human Subjects Committee. Samples were collected from 50–80 years old females diagnosed with no cancer or with stage I–IV ovarian cancer of various histological subtypes. The detailed population information is provided in Table S2.

Recruitment

No recruitment was necessary.

